Ore Geology Reviews 78 (2016) 14–40

Contents lists available at ScienceDirect

Ore Geology Reviews

journal homepage: www.elsevier.com/locate/oregeorev

A secondary precious and base metal mineralization in chromitites linked to the development of a Paleozoic accretionary complex in Central Chile

José M. González-Jiménez [a,*], Fernando Barra [a], Leonardo N.F. Garrido [a], Martin Reich [a], Takako Satsukawa [b,c], Rurik Romero [a], Eduardo Salazar [a], Vanessa Colás [d], Felipe Orellana [a], Osvaldo Rabbia [e], Gaëlle Plissart [f], Diego Morata [a]

[a] Department of Geology and Andean Geothermal Center of Excellence (CEGA), Universidad de Chile, Plaza Ercilla # 803, Santiago de Chile, Chile
[b] ARC Centre of Excellence for Core to Crust Fluid Systems (CCFS), and GEMOC National Key Centre, Department of Earth and Planetary Sciences, Macquarie University, Sydney, NSW 2109, Australia
[c] Department of Geophysics, Division of Earth and Planetary Sciences, Kyoto University, Kyoto 606-8502, Japan
[d] Instituto de Geología, Universidad Nacional Autónoma de México, Ciudad Universitaria, 04510 Mexico, D.F., Mexico
[e] Instituto de Geología Económica Aplicada,, Universidad de Concepción, Concepción, Chile
[f] Instituto de Ciencias de la Tierra, Universidad Austral de Chile, Valdivia, Chile

ARTICLE INFO

Article history:
Received 26 November 2015
Received in revised form 17 February 2016
Accepted 24 February 2016
Available online 16 March 2016

Keywords:
Precious metals
Chromite
Serpentinite
Metamorphism
Accretionary complex

ABSTRACT

Platinum-group element (PGE) and gold inclusions are usually present in peridotites and chromitite deposits associated with ophiolites. Here, we present the first detailed study of the mineralogy of precious metals in ultramafic rocks hosted in the Paleozoic Coastal Accretionary Complex of Central Chile. In these ultramafic rocks the mineralization of precious metals is associated with small meter-size pods and veins of massive chromitite hosted in serpentinite-filled shear zones. Crystallographic orientation maps of single chromite grains, obtained using the Electron-Backscattered Secondary Diffraction technique, allow us to identify two types of chromite in the precious-metal bearing chromitites: (1) Type A chromite, characterized by an average misorientation per grain of ≤2° and chemically homogeneous cores surrounded by a porous rim with abundant inclusions of chlorite, and (2) Type B chromite, which exhibits higher degrees of misorientation (2–8°) and porosity, and abundant silicate inclusions, but a relatively homogeneous chemical composition. In situ analyses using EMPA and LA-ICP-MS for major, minor and trace elements indicate that composition of the magmatic chromite is only preserved in the cores of Type A chromite grains. Core to rim chemical trends in these Type A chromites are characterized by a progressive increase of the Cr# with a decrease of the Mg#, loss of Al and addition of Fe^{2+} in the porous rim. The observed changes in the microstructure and chemistry of chromite are associated with the infiltration of external fluids through shear zones filled with antigorite (±talc) developed in partly serpentinized peridotites (i.e., olivine–lizardite dunites). Thermodynamic calculations using the phase equilibria relations in the system Cr_2O_3–MgO–FeO–Al_2O_3–SiO_2–H_2O (CrMFASH) indicate that Fe^{2+}-rich porous chromite + chlorite replaced the original assemblage chromite + olivine in the chromitite while prograde antigorite was formed. According to our results this transformation occurred at ~510–560 °C when external fluids penetrated the ultramafic/chromitite bodies through shear zones. These temperatures are slightly higher than estimated for the metamorphic peak in the host metapelitic rocks (i.e., ~420 °C at 9.3 kbar), suggesting that a hotter ultramafic body was captured by the metasediments of the accretionary prism during their exhumation through subduction channel. Chlorite geothermometry yielded a wide range of lower temperature from 430 to 188 °C, for chlorite present in the porous chromite rims. These results are in agreement with the retrograde overprint under greenchist-facies metamorphism conditions recorded by metapelitic host rocks and minor volcanogenic massive sulphide deposits in the area (300–400 °C, ~3–4 kbar). We suggest that although initially decoupled, the chromitite-bearing ultramafic rocks and their metasedimentary host undergone a common metamorphic PT pathway of exhumation during the formation and evolution of the subduction-related accretionary complex.

The chromitites contain appreciable amounts of the platinum-group elements (up to 347 ppb total) and gold (up to 24 ppb), present as inclusions of platinum-group minerals (PGM) and alloys as well as native gold. The PGM identified include native osmium, laurite (RuS_2), irarsite (IrAsS), osarsite (OsAsS), omeiite ($OsAs_2$), Pt–Fe alloy (possibly isoferroplatinum) and a suite of inadequately identified phases such as PtSb (possibly stumpflite), PdHg (possibly potarite), RhS, Ir–Ni and Ir–Ni–Ru compounds. Only a few grains of osmium and laurite were identified in unaltered cores of chromite and therefore considered as magmatic in origin formed during the high-T event of chomite crystallisation in the upper mantle. The other PGM were located in the porous chromite

* Corresponding author at: Universidad de Chile, Departamento de Geología, Plaza Ercilla # 803, Santiago de Chile, Chile.
E-mail address: jmgonzj@ing.uchile.cl (J.M. González-Jiménez).

http://dx.doi.org/10.1016/j.oregeorev.2016.02.017

associated with chlorite or base-metal minerals (BMM) that often fill the pores of this altered chromite or are intergrowth with antigorite in the host serpentinized ultramafic rock. The assemblage of BMM identified in the studied rocks include sulphides [millerite (NiS), polydymite (Ni_3S_4), violarite ($FeNi_2S_4$), galena (PbS), sphalerite (ZnS), chalcocite (CuS)], arsenides [(orcelite ($Ni_{5-x}As_2$) and maucherite ($Ni_{11}As_8$)], the sulpharsenide gersdorfitte (NiAsS), and native bismuth. The irregular shape of several PGM grains observed in porous chromite suggest disequilibrium, whereas others exhibit perfectly developed crystal faces with the associated secondary silicate or base-metal mineral suggesting *neoformation* of PGMs in situ from metamorphic fluids. We suggest that the origin of these PGM inclusions is magmatic, but some grains were reworked in situ when metalloid (i.e., As, Sb, Pb, Zn and Hg)-rich fluids released from metasediments penetrated the ultramafic rocks through active shear zones, once the ultramafic bodies became tectonically mixed with the host metasedimentary host rocks. During this event, gold sourced from the (meta)sediments was also precipitated within chromitites and serpentinites.

1. Introduction

The Chilean Coastal Cordillera extends almost continuously between latitude 32°S and 43°S along the Pacific coast of Chile (Fig. 1a). It is interpreted as an accretionary complex developed at the southwestern margin of Gondwana during the Late Paleozoic (Hervé et al., 1976; Hervé, 1977; Godoy, 1979; Hyppolito et al., 2014a,b). This complex comprises two paired units or metamorphic belts known as the Western Series (to the West) and the Eastern Series (to the East), which were affected by metamorphism at high and low P/T ratios, respectively (Aguirre et al., 1972; Hervé et al., 1988; Willner et al., 2005; Richter et al., 2007; Glodny et al., 2008; Hyppolito et al., 2014a). In the 1960s the Canadian company Lockwood conducted an exploratory geophysical survey across the Coastal Cordillera, which identified numerous magnetic anomalies in the southern part of the Western Series. These anomalies were preliminarly interpreted as iron ores and triggered numerous subsequent lithological and structural studies.

In 1970, researchers of the *Instituto de Investigaciones Geológicas* developed an extensive field campaign in order to identify the cause of these aeromagnetic anomalies (Lockwood Survey Co., 1969). They concluded that some of these magnetic anomalies were not produced by iron ores but that they corresponded to bodies of mafic and ultramafic rocks containing appreciable amounts of iron-bearing minerals (Álvarez and Rivera, 1970; Vergara, 1970). A decade later, Alfaro (1980, 1981) identified chromite ores in the ultramafic body of Lavanderos in the La Cabaña area, approximately 60 km from the city of Temuco (Fig. 1a). Although the aforementioned chromite ores were small and rejected as an economic source of chromium, Alfaro (1980, 1981) observations were a landmark for subsequent studies published at the end of the 90s (Barra et al., 1998; Höfer et al., 2001). These more recent studies provided better constraints on the petrography and composition of the chromite ores and their host rocks cropping out in the area of La Cabaña. However, a detailed interpretation regarding the mechanism(s) of crystallisation and the setting of formation of these chromite ores was not aimed in these studies.

Recently, González-Jiménez et al. (2014a) have used the composition of chromite coupled with the bulk-rock platinum-group elements (PGE) and Re–Os isotopes of the chromite ores from La Cabaña to confirm an ophiolitic origin. They also proposed that the chromite ores were formed beneath a spreading center developed above a suprasubduction zone, in which arc-type melts would mingle within dunite conduits representing channels for the extraction of these melts. Meanwhile, Barra et al. (2014) showed that the infiltration of postmagmatic fluids during regional metamorphism promoted the reaction of magmatic chromite with the olivine matrix, producing rims of secondary Fe^{2+}-rich porous chromite in equilibrium with chlorite.

The data provided by González-Jiménez et al. (2014a) indicate that the chromite ores from La Cabaña concentrated mainly Os, Ir and Ru, producing the negative slope that ophiolitic chromitites characteristically show in the chondrite-normalised PGE patterns. These results are consistent with the presence of few grains of Os–Ir-rich alloys and sulpharsenides identified by Galdames et al. (2011). It is accepted that Os–Ir-rich PGMs can be genetically linked with the crystallisation of chromite at relatively high temperature from basaltic melts (Mungall, 2005; Finnigan et al., 2008; González-Jiménez et al., 2009; Uysal et al., 2009; Pagé et al., 2012). However, they can be also formed by the alteration of pre-existing PGMs or by direct re-precipitation of PGE mobilised during the metamorphic alteration of chromite (Proenza et al., 2008; El Ghorfi et al., 2008; Prichard et al., 2008; Tsoupas and Economou-Eliopoulos, 2008; González-Jiménez et al., 2010). The fact that the chromite ores of La Cabaña underwent significant modification during regional metamorphism suggests a feasible scenario for the formation of a secondary precious metal mineralization. However, the knowledge of the PGE + Au mineralization in the La Cabaña chromite ores is still rudimentary because there is no detailed characterization of the genetic and spatial relationships of unaltered vs. altered chromite, and the potential PGE mineral carriers.

In this contribution, we performed an extensive study of the mineralogy of the platinum-group elements and gold, and their accompanying base-metal minerals (BMM, including sulphides, sulpharsenides, arsenides and antimonides) and silicates found as inclusions in the chromite ores. In addition we undertook a detailed study of the microstructure of the precious metal-bearing chromitites as well as original bulk-rock data for the chromite ores (including PGE + Au). These microstructural and geochemical data were coupled with field observations, and integrated within the framework of a new structural map of the ultramafic bodies, aimed at evaluating the role of shear zones (in partly serpentinized peridotites) on chromite alteration.

In addition, crystallographic orientation maps of single chromite grains, obtained using the Electron-Backscattered Secondary Diffraction (EBSD) technique, were collected to constrain the micro-structural relations between deformation and alteration at the scale of small chromite grains. Furthermore, new EMPA and LA-ICPMS analyses carried out on individual grains of chromite and associated silicates were used to fingerprint the metamorphic signal of chromite and to refine our previous estimates of the PT conditions for the PGM (chromite) host alteration. Finally, these results are used to establish the evolutionary stages of precious metal mineralization within the framework of the Accretionary Complex developed in the Coastal Cordillera of Central Chile during the Paleozoic. In a broad sense, our study constraints the interplay between deformation and fluid infiltration in the formation of precious and base metals ores during regional metamorphism of ultramafic rocks.

2. Geological background

2.1. The Coastal Cordillera of south-central Chile

The Coastal Cordillera of south-central Chile (Fig. 1a) comprises two parallel N–S trending metamorphic belts, the so-called Western and the Eastern series, characterized by different metamorphic gradients and rock assemblages. The Eastern Series comprises slightly deformed

sedimentary rocks (graywackes and metapelites) affected by high-temperature and low- to intermediate pressure metamorphism. In contrast, the rocks of the Western Series were metamorphosed under higher pressure and lower temperature conditions. These are rocks of continental origin formed in a passive margin and/or trench (metapelites and metapsammites) intermingled with rocks of oceanic affinity (greenschists, blueschists, amphibolites, metasediments, metavolcanics, metagabbros and metaperidotites). Some of the Western Series rocks were deformed and metamorphosed together with the surrounding host formations (Aguirre et al., 1972; Hervé, 1977; Frutos and Alfaro, 1987; Barra et al., 1998; Höfer et al., 2001; Willner et al., 2001; Glodny et al., 2005; Hyppolito et al., 2014a,b). The Western Series has been divided in two sections: the northern (34–36°S) and southern section (38–43°S; Fig. 1a). The metamorphic peak conditions estimated for the rocks of the northern section are 7.0–9.3 kbar and 380–420 °C, although scattered outcrops of blueschists preserve a record of higher pressures (9.5–10.7 kbar) at lower temperature (350–385 °C) (Willner, 2005). Willner et al. (2001) and Glodny et al. (2005) have estimated similar peak metamorphic conditions for metasedimentary rocks in a few localities of the southern section of

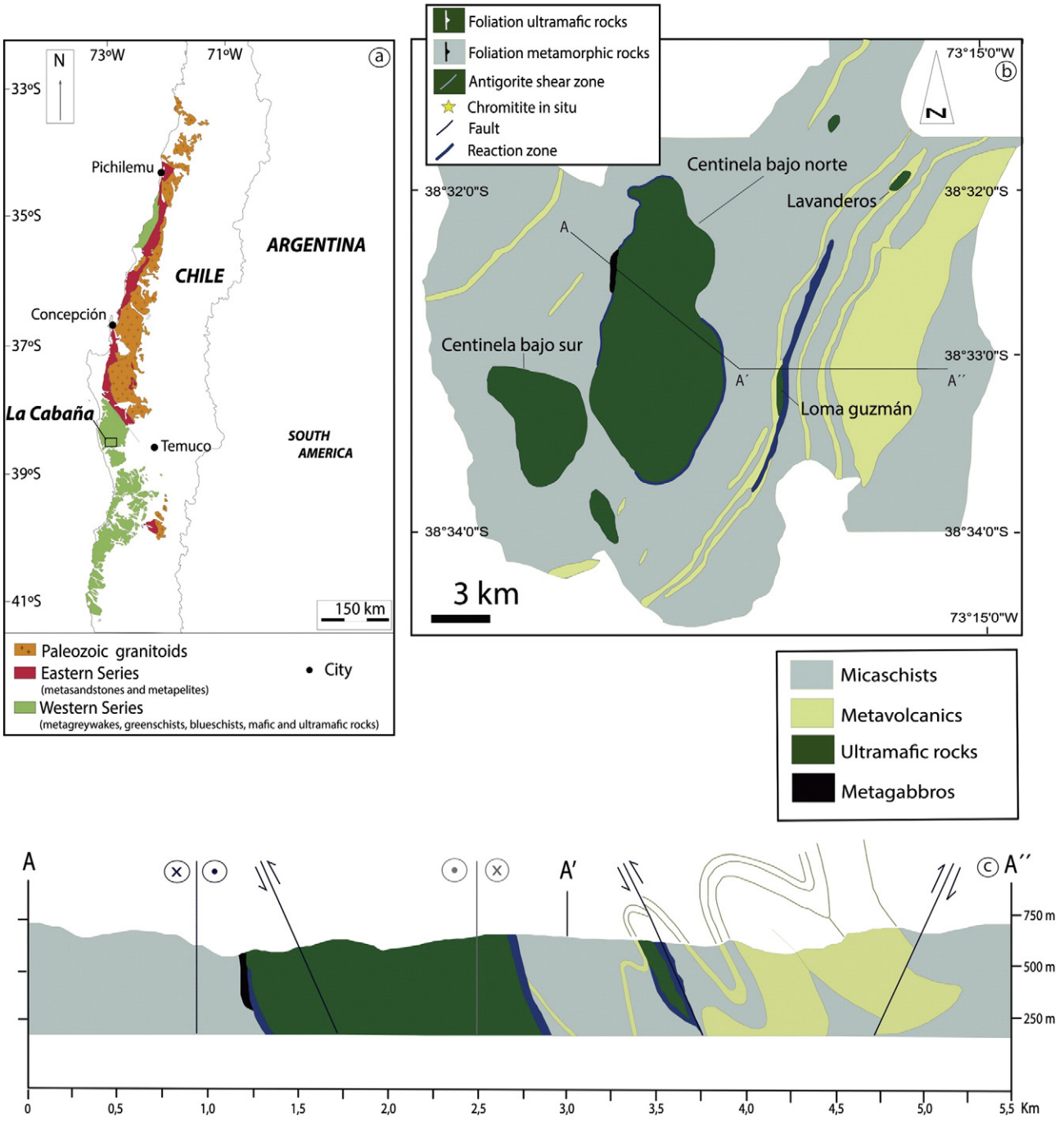

Fig. 1. Location of the La Cabaña area in the Coastal Cordillera of South Central Chile (a), main lithotectonic units (b), and cross-section from (b) (c) showing the relation between the ultramafic rocks and their country rock.
Modified from Höfer et al. (2001) and Hervé et al. (2013).

the Western Series at Bahia Mansa (i.e., 6–8 kbar and 270–370 °C) and Valdivia areas (8–9 kbar and 420 °C). A late metamorphic event under greenschist-facies conditions (~3–4 kbar and 300–400 °C) overprinted the HP/LT metamorphism assemblages throughout the entire belt.

The assemblage of metabasites, serpentinites and metacherts identified in the Western Series has been interpreted as a dismembered ophiolite complex (Hervé, 1974; Barra et al., 1998; Höfer et al., 2001; González-Jiménez et al., 2014a). Studies based on the amphibolites in the Pichilemu region at the northern part of the Western Series have led some authors to suggest that these ophiolitic rocks were exhumed, and later emplaced on the paleomargin of Gondwana, by basal and frontal accretion processes in a paleo-subduction channel during the Late Paleozoic (Willner, 2005; Hyppolito et al., 2014a). However, an alternative model based on the study of metabasites, metaperidotites and metacherts cropping out in the southernmost part of the Coastal Cordillera (i.e., south Lanalhue Fault Zone, ~38°S) suggests that these ophiolitic rocks originated in a marginal basin developed in a back-arc setting (Frutos and Alfaro, 1987; Vivallo et al., 1988; Schirra, 1991; Rabbia et al., 1994; Höfer et al., 2001). More recently, González-Jiménez et al. (2014a) suggested that the peridotites from La Cabaña area could represent volumes of ancient Subcontinental Lithospheric Mantle (SCLM) that was modified during oceanization processes associated with the opening of a marginal basin above a suprasubduction zone (SSZ).

To the best of our knowledge, only two of these bodies of peridotites at La Cabaña host chromite ores (hereafter chromitites), and they are sub-economic. The chromitite samples for this investigation were collected from shear zones in the metaultramafic bodies of Centinela Bajo and Lavanderos in the La Cabaña area (Fig. 1b).

2.2. Ultramafic bodies of the La Cabaña area

2.2.1. Centinela Bajo

The Centinela Bajo area is located north of the El Encanto river, near the town of Trovolhue, and comprises two outcrops of metaperidotites defined here as Centinela Bajo Norte and Centinela Bajo Sur (Fig. 1b). These ultramafic bodies are hosted by metasedimentary rocks (Vergara, 1970; Alfaro, 1980; Barra et al., 1998; Höfer et al., 2001; Barra et al., 2014; González-Jiménez et al., 2014a).

The ultramafic bodies are covered by a thick lateritic soil on which a dense rainforest has developed, which gives little opportunity for direct observation of outcrops. The field observations reported below were performed in good exposures of the ultramafic rocks at three different sections of the Centinela Bajo Norte body (6 km long and 3 km wide): Loma de las Ovejas (easternmost part of the body), Loma Rurik (westernmost part) and Río de las Vacas (northern part; Fig. 2). Despite the poor exposure, our detailed mapping reveals that shear zones control the internal structure of this ultramafic body (Fig. 2). These are identified in the field by bands of schistose serpentinite that comprises antigorite ± talc ± tremolite ± magnetite (Fig. 3a). These shear zones surround and isolate blocks of dunites with lenses of harzburgite. Mantle foliation is defined in the peridotites by trails of Cr-spinel or pyroxene in the now porphyroclastic rock. This foliation strikes N 20–40°E, dipping 30–50°E, but is parallel to the orientation of the mylonitic serpentinite filling the shear zones. Dunite, by far the predominant protolithic rock in the body, contains coarse-grained porphyroclastic olivine (1–2 mm) replaced by pseudomorphic (mesh texture) lizardite, with minor amounts of pyroxene and Cr-spinel partly replaced by Fe^{2+}-rich porous chromite rims and/or magnetite (Barra et al.,

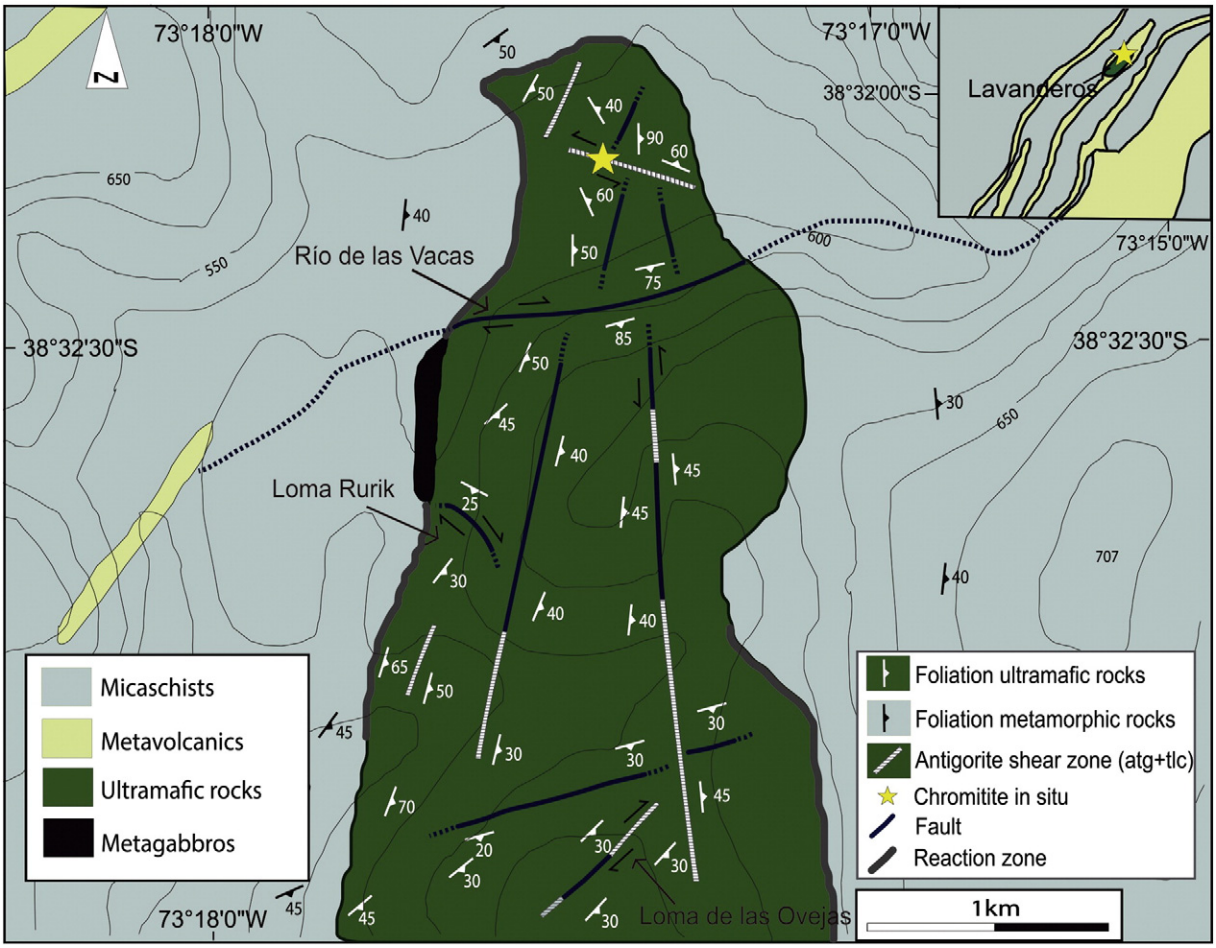

Fig. 2. Simplified geological map of La Cabaña ultramafic bodies showing the location of the two chromitite sites investigated in this work.

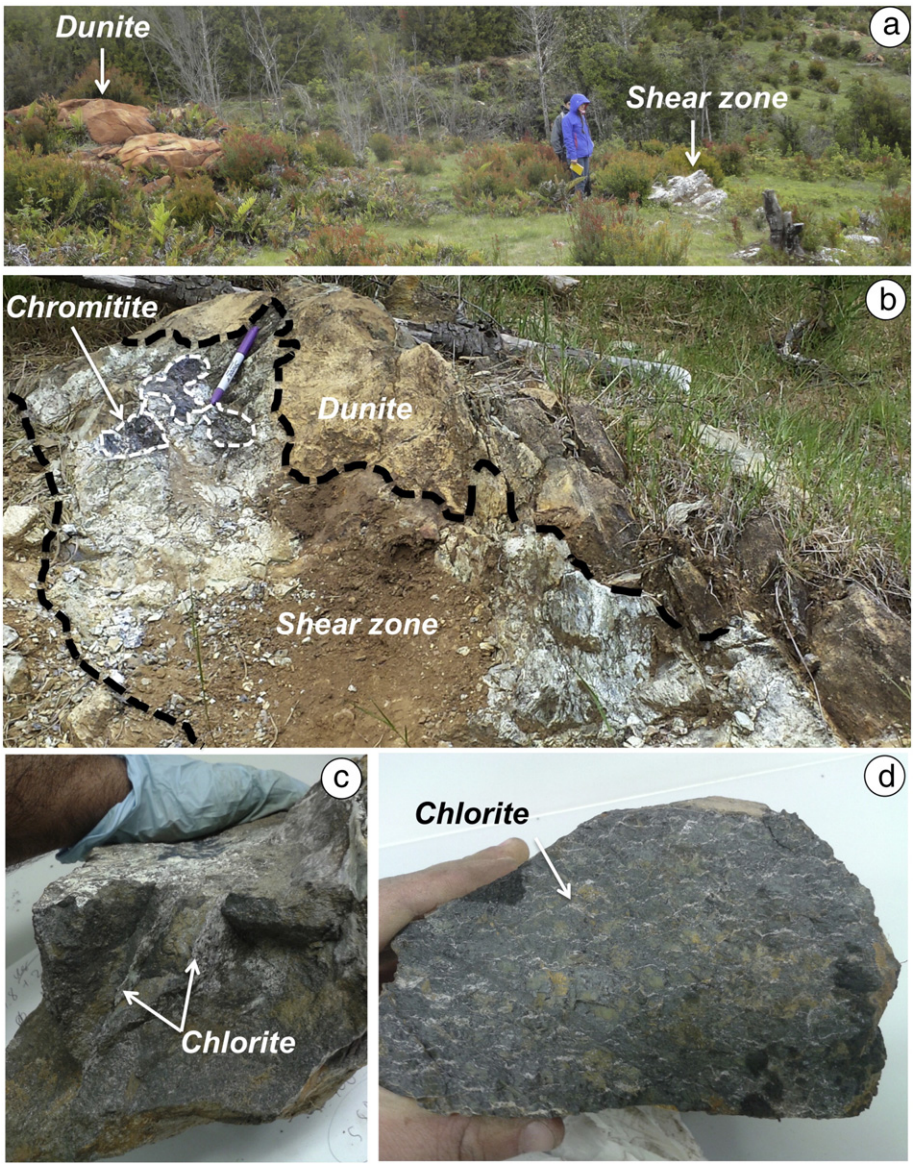

Fig. 3. Photographs showing field relationships of different rocks within the La Cabaña ultramafic bodies. Centinela Bajo Norte (a–d), Lavanderos (e–h).

2014). The secondary mineralogy includes chlorite and amphibole, and a late generation of chrysotile and Mg-carbonate veins crosscut all of the described minerals.

Several authors have reported boulders of chromitite in both Centinela Bajo Norte and Centinela Bajo Sur bodies (Barra et al., 1998; Höfer et al., 2001; González-Jiménez et al., 2014a). These irregular boulders are relatively large (>50 cm long), consist of massive chromitite (>90% chromite) with minor Cr-rich chlorite, and were found along the drainage system. Höfer et al. (2001) interpreted them as fragments derived from a hidden larger chromitite body, which were eroded and transported to the drainage system during active flooding. However, and despite our efforts during several fieldwork campaigns, we did not find outcrops at the top of the hills (i.e., the potential source). However, we identified outcrops of in-situ chromitites at the bottom of streams draining the hills of Río de las Vacas at the Centinela Bajo Norte body (Figs. 2 and 3b). These observations led us to suggest that the boulders of chromitites described in previous works could be "chromitite floaters" liberated mechanically from their bedrock during the weathering of the ultramafic rocks. Once detached from their host rocks, these chromitite floaters would be uplifted mechanically towards the surface. This has been previously described in the lateritic soils developed on ophiolitic rocks from Cuba (e.g., Thayer, 1942) and the Dominican Republic (Aiglsperger et al., 2015).

This new chromitite outcrop we identified in-situ was observed north of the Río de las Vacas, and it is associated with an antigorite (±talc) shear zone. It is a small body (<1 m long and 50 cm wide) with an irregular shape that shows sharp contacts with the host dunite (Fig. 3b). Interestingly, some parts of the chromitite–serpentinite contact show a dense, ferruginous and siliceous rock that displays clear evidence of pseudomorphic replacement of the protolith by quartz. This type of rocks has been described in the literature as "birbirite" (Glennie et al., 1974). At hand-specimen scale, the chromite ores exhibit strong deformation characterized by brittle fractures filled with chlorite (Fig. 3c), or preferential orientation of strained chromite grains within the chlorite groundmass (Fig. 3d).

2.2.2. Lavanderos

The ultramafic body of Lavanderos (200 m long and 35 m wide) is also in direct tectonic contact with metasedimentary rocks (Figs. 1b and 2). They are almost completely composed of antigorite (±talc) with accessory chlorite and disseminated chromite altered to iron-rich

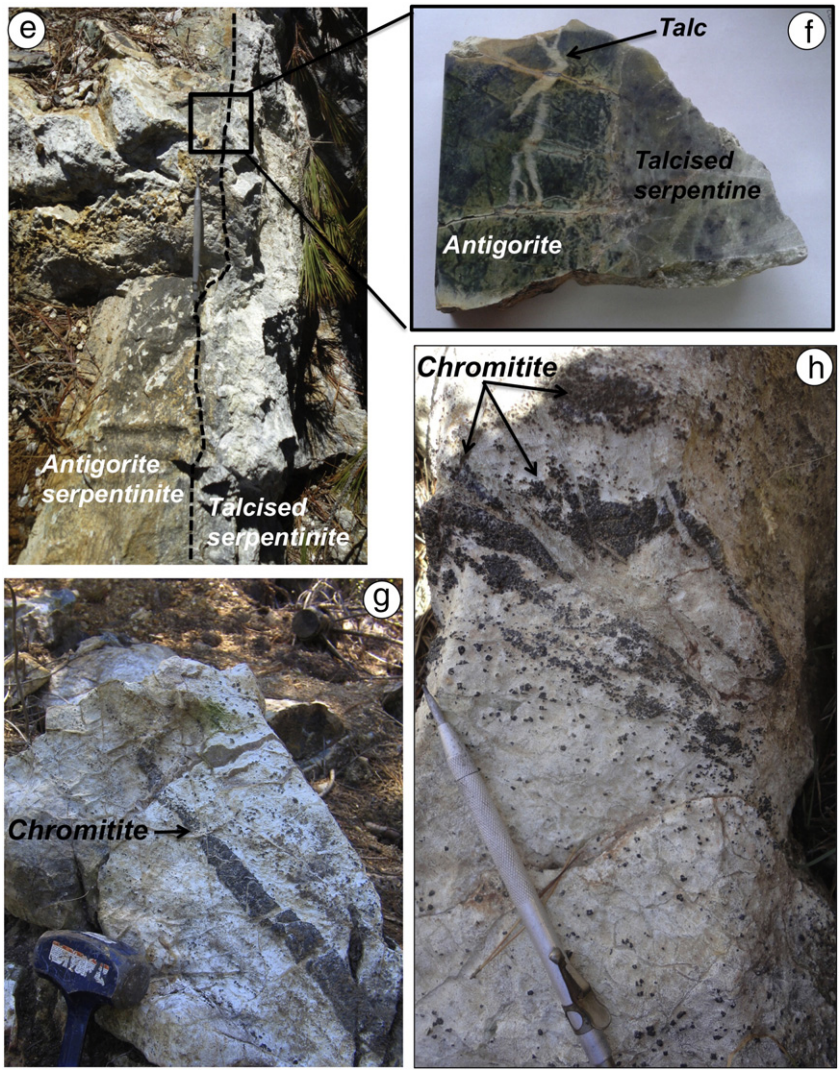

Fig. 3 (*continued*).

chromite (Barra et al., 1998; Höfer et al., 2001). Talc locally replaces both antigorite and chlorite in pseudomorphic microstructures or forms veinlets disrupting the serpentinite (Fig. 3e–f). Based on field relations, mineralogical constraints and whole-rock geochemistry of the serpentinite (see below), we consider Lavanderos outcrop as a shear zone similar to those identified at the neighbouring Centinela Bajo Norte body, which was very likely detached from this larger body during its tectonic emplacement into the upper crust. Shearing and fault-controlled emplacement into the crust have developed a characteristic penetrative mylonitic foliation towards the boundaries of the body. A later event of metasomatism characterized by the infiltration of Si-rich fluids from the metasedimentary host rocks, has produced a well developed reaction zone of talc and an outer zone of actinolitite along the contact with the micaschist (Fig. 3f; Höfer et al., 2001).

The chromitites at Lavanderos are lenses and veins of a few centimetres thick that are hosted in the serpentinite with the greater degrees of talcisation (Fig. 3g–h). The contact between the chromitite and the host often is sharp but the massive chromitite can locally grade to a disseminated chromitite through a zone of schlieren chromite (Fig. 3h). Frequently, late veins of both talc and chrysotile cut the chromite veins, disrupting their continuity.

3. Analytical methods

3.1. Bulk-rock trace element of serpentinites and PGE geochemistry of chromitites

Clean rock samples of serpentinites were analysed by Acme Analytical Laboratories, Vancouver, Canada for major, minor and trace elements. Samples were crushed, pulverized in ceramic bowl, later decomposed in multiacid solutions and analysed using ICP-MS.

Six chromitite samples were analysed for bulk contents of platinum-group elements (PGE) and gold. The analyses were performed at Actlabs, Canada, using nickel sulphide fire assay and instrumental neutron activation analysis (INAA) techniques. Detection limits were 5 ppb for Ru and Pt, 2 ppb for Os and Pd, 0.5 ppb for Au, 0.2 ppb for Rh, and 0.1 for Ir.

3.2. Microstructural analysis of chromite (EBSD and EDS analysis)

In order to evaluate the mineral fabric characteristics of the chromitites, crystallographic orientations were measured using the SEM (Scanning Electron Microscopy)-EBSD (Electron Backscattered Secondary Diffraction) facility in the Geochemical Analysis Unit (GAU)

Facility of the ARC (Australian Research Council) Centre of Excellence for Core to Crust Fluid Systems (GEMOC, Macquarie University, Australia). The EBSD patterns were generated by the interaction of a vertical incident electron beam with a polished thin section, tilted at 70° to the horizontal in a scanning electron microscope (Zeiss EVO MA15). The operating conditions were: 20 kV, 8.2 nA and working distance of 12.0–13.0 mm. The diffraction patterns were projected onto a phosphor screen and recorded using a digital CCD camera. The resulting image was then processed and indexed in terms of crystal orientation using the CHANNEL5 software distributed by Oxford Instruments. Maps were acquired with sampling step size of 2 or 10 μm depending on the mean grain size. Post-acquisition data processing includes the extrapolation of well-indexed neighbouring points to non-indexed points, and removal of grains (as defined by continuous domains characterized by an internal misorientation <10°) smaller than 5 pixels in average diameter.

3.3. Mineral chemistry

Polished thin sections of chromite were inspected at the Electron Microscopy Laboratory, Andean Geothermal Center of Excellence, CEGA (University of Chile) using a FEI Quanta 250 scanning electron microscope (SEM) equipped with energy-dispersive spectrometry and a back-scattered electron (BSE) detector. The preliminary semiquantitative compositions of grains of chromite and their hosted silicates, PGM, and BMM were obtained using energy-dispersive (EDS) analysis. Major- and minor-element compositions of chromite, silicates, PGM and BMM grains were obtained by wavelength-dispersive spectrometry (WDS) analysis using a JEOL JXA-8230 at the Centres Científics i Tecnològics of the University of Barcelona (CCiTUB, Barcelona, Spain). An accelerating voltage of 15 keV and a beam current of 20 nA were used. All elements were measured with a counting time of 10 s for the peak. Calibration for analysis was performed using natural and synthetic standards. The standards used for chromite and silicate analyses were: diposide for SiO_2, rutile for TiO_2, periclase for MgO, corundum for Al_2O_3, Fe_2O_3 for FeO, rhodonite for MnO, sphalerite for ZnO, NiO for NiO, metallic Co for Co, and chromite for Cr_2O_3; the X-ray lines used were the Kα for all the elements. The analysis of the base-metal minerals (including sulphides, arsenides and sulpharsenides) were calibrated against natural FeS for S and Fe, PbS for Pb, chalcopyrite for Cu, and chromite for Cr, synthetic InSb for Sb and GaAs for As, and metallic Co for Co and metallic Ni for Ni; the X-ray lines employed were Kα for S, Fe, Co, Ni and Cr, Mα for Pb and Lα for Sb and As. Pure metals were used as standards for Os, Ir, Ru, Rh, Pt, Pd, Co and Ni as well as GaAs for As, FeS_2 for S and Fe, and chalcopyrite for Cu during the analysis of platinum-group minerals. The X-ray lines used were Kα (for S, Fe, Co, Cu, Ni and Cr), Mα (for Os), Lα (for As, Pt and Ir, Ru and Rh), and Lβ (for Pd). In the analytical routine for EMPA analysis of platinum-group minerals and base-metal minerals, Si, Cr and Fe were included to evaluate the quality of the performed analyses on very small grains (hosted in silicates or chromite). When PGMs were hosted in chromite, the raw EMPA data were corrected by subtraction of Cr and the corresponding proportion of Fe (determined from the known Cr/Fe ratio, measured in the host chromite), and the atomic concentration was calculated from the corrected analytical data (González-Jiménez et al., 2009).

3.4. LA-ICP-MS analysis of chromite

The trace element composition of chromite was quantitatively determined using Laser Ablation-Inductively Coupled Plasma-Mass Spectrometry (LA-ICP-MS). In situ analyses were performed using a 193 nm Photon Machines Ecite excimer laser ablation system coupled to an Agilent 7500cs ICP-MS in the Geochemical Analysis Unit of CCFS/GEMOC, Macquarie University, Sydney, Australia. The following masses were measured: ^{45}Sc, ^{47}Ti, ^{51}V, ^{55}Mn, ^{59}Co, ^{60}Ni, ^{66}Zn, and ^{71}Ga. The isotopes ^{29}Si and ^{42}Ca were monitored to check for the presence of silicate inclusions.

The analyses were conducted using an ~30–50 μm beam diameter, 5 Hz frequency, and 0.158 mJ/pulse power during 180 s analysis (60 s for the gas blank and 120 s on the ablated chromite). The instrument was calibrated against the NIST 610 silicate glass (National Institute Standards and Technology, Gaithersburg, USA; Norman et al., 1996). The basaltic glass BCR-2g (Norman et al., 1998; Gao et al., 2002) and the in-house secondary standards LCR-1 and LCR-2 (Lace mine, South Africa; Locmelis et al., 2011) were analysed as unknowns during each run to check the accuracy and precision of the analyses. Aluminium concentrations determined previously using electron microprobe were used as the internal standard and the data obtained during ablation runs were processed using the GLITTER software (Griffin et al., 2008).

4. Results

4.1. Geochemistry and mineralogy of the serpentinite host rocks

4.1.1. Bulk contents of transition metals in serpentinites

In order to constrain the geochemical effects of serpentinization on the original magmatic signature of ultramafic rocks at La Cabaña, we analysed a suite of minor and trace elements (Sc, Ti, V, Cr, Co, Ni, Cu, Zn, Cd, Lu, As, Sb, Pb, Ba, Sr) in peridotites with different styles and degrees of serpentinization. The results are plotted in Fig. 4 and listed in Table 1.

Fig. 4 shows the bulk-rock concentrations normalised to the depleted mantle using the values reported by Salters and Stracke (2004), and plotted against increasing mobility in hydrothermal fluids (typical of serpentinization processes). Overall, both the olivine–lizardite dunites and antigorite (±talc) serpentinite show patterns similar to those of mantle wedge serpentinites with dunite protolith (grey field in Fig. 4; Deschamps et al., 2013). However, our samples show remarkably lower concentrations of Li, Co and Ni, but higher Sb, Pb and Ba, particularly the schistose antigorite (±talc) serpentinite filling shear zones. If one observes only the distribution of these Fluid Mobile Elements (FME, Deschamps et al., 2011) it is noted that there are differences between the olivine–lizardite dunites (only in the Centinela Bajo Norte body) and the antigorite (±talc) serpentinite filling the shear

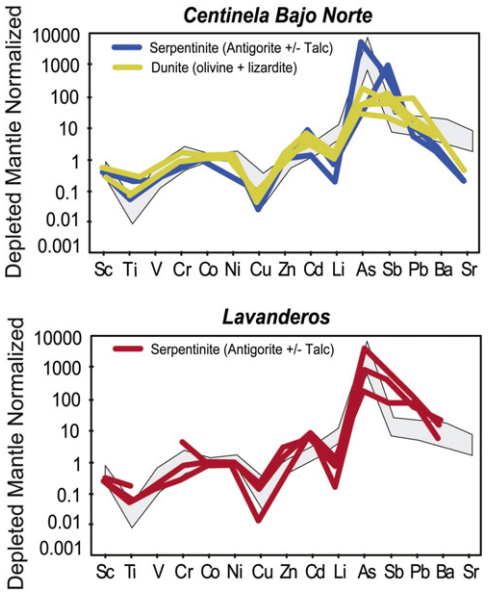

Fig. 4. Trace element patterns for the ultramafic rocks of the La Cabaña area. The graphed values were normalised to the depleted mantle using the values reported by Salters and Stracke (2004). Grey field are mantle wedge serpentinites with dunite protolith (Deschamps et al., 2013).

Table 1
Whole-rock analyses of major, minor and trace elements in serpentinites and partly serpentinised peridotites from the La Cabaña ultramafic bodies (in ppm).

Sample	Sc	Ti	V	Cr	Co	Ni	Cu	Zn	Cd	Li	As	Sb	Pb	Ba	Sr	Cs	U
Centinela Bajo Norte																	
CAB-11C	54.5	5490	249	1122	79.8	644.7	31.71	48.9	0.06	12.4	3.2	0.03	0.51	5	15	<0.1	<0.1
CAB-12B	6.50	120	15	1400	112.5	2585.6	0.8	32.4	<0.02	0.4	0.4	0.17	0.22	3	<1	<0.1	<0.1
PODOA	6.90	30	17	2018	108.2	2391.3	1.08	53.2	0.02	0.1	36.8	1.01	0.29	2	<1	<0.1	<0.1
CAB-7C	4.30	40	15	3814	113.2	2398.5	2.1	55.4	0.06	0.4	15.7	2.43	0.13	2	2	<0.1	<0.1
CAB-12	6.40	50	18	2461	111.1	2525.4	0.62	40.6	0.04	0.9	0.4	0.35	0.39	6	<1	<0.1	<0.1
CAB-13	4.70	30	10	1054	116.6	2479.5	1	33.5	0.13	<0.1	<0.2	0.06	0.08	3	2	<0.1	<0.1
CAB-14	7.20	120	27	3781	108.1	2428.7	1.2	49.7	0.04	0.5	0.2	0,06	0.21	6	4	<0.1	<0.1
Lavanderos																	
LAV	6.70	10	11	661	76.9	1693.1	0.33	23.9	0.1	0.1	6.7	1.04	1.29	24	<1	<0.1	<0.1
LAV-R	6.90	30	14	1752	97.9	1960.7	3.12	71.8	0.1	0.8	1.3	0.2	1.92	6	<1	<0.1	<0.1
LAV-3	4.30	120	<1	10,000	105.7	1910.9	6.15	164.7	0.08	0.5	35.5	1.83	2.5	16	<1	<0.1	<0.1
CAB-14	7.20	120	27	3781	108.1	2428.7	1.2	49.7	0.04	0.5	0.2	0.06	0.21	6	4	<0.1	<0.1

zones. The latter show the lowest values of Li and the highest concentrations of As, Sb, and Pb.

4.1.2. Ni-arsenides in the serpentinites

A few composite grains consisting of intergrowths of awaruite (Ni_3Fe) and heazlewoodite (Ni_3S_2) were identified in the olivine–lizardite dunites. In contrast, the relatively high contents As in the antigorite (±talc) serpentinite filling the shear zones have their mineralogical expression in the presence of numerous (>50 μm in diameter) grains of Ni-rich arsenides (orcelite [$Ni_{5-x}As_2$] and maucherite [$Ni_{11}As_8$]) intergrown with antigorite (Fig. 5a–d) or filling interstices in secondary porous chromite rims (Fig. 5e–f).

Orcelite (n = 64; Appendix 1) in the studied serpentinites is very homogeneous and has a structural formula close to stoichiometric [$Ni_{4.99}As_2$ to $Ni_{4.54}As_2$] with very limited Co (up to 0.87 wt%) and Fe (up to 4.5 wt%) substitution for Ni, and Sb for As (up to 5 wt%). In contrast, the composition of maucherite (n = 3; Appendix 1) deviates from the ideal stoichiometry due to the presence of noticeable amounts

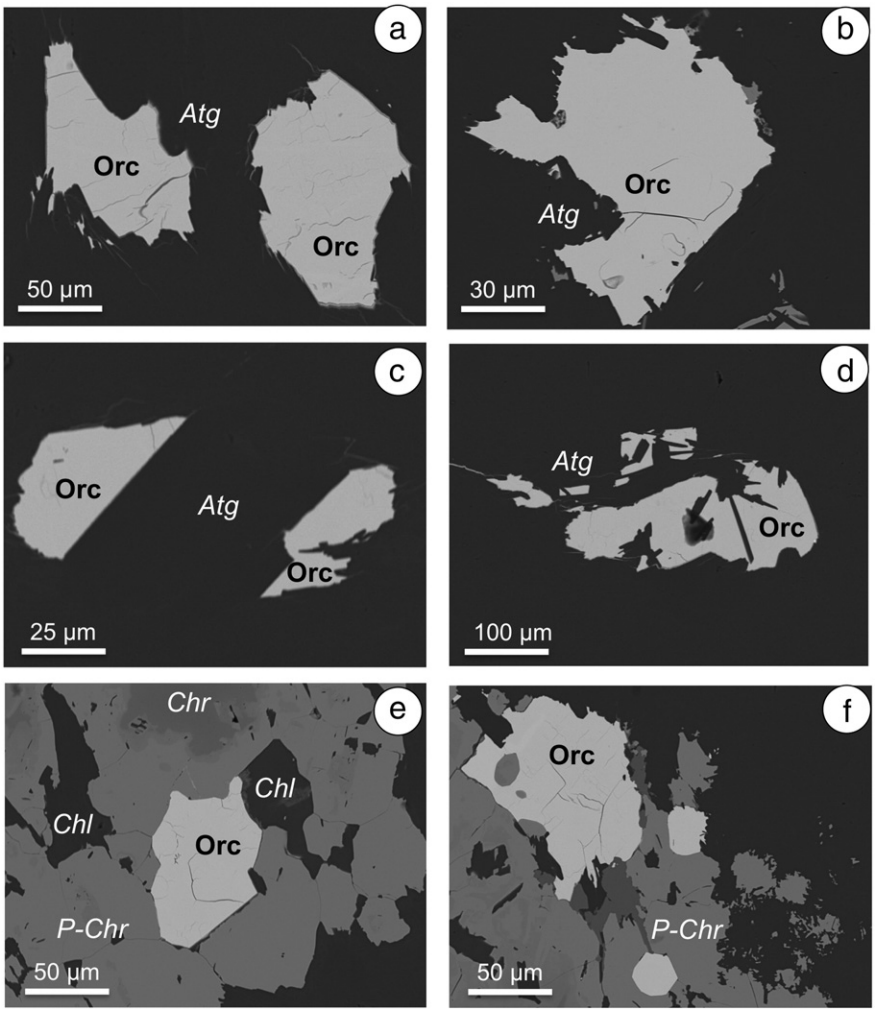

Fig. 5. Backscattered electron images of Ni-arsenide orcelite in schistose antigorite (±talc) serpentinite from the La Cabaña shear zones. Abbreviations: Atg: antigorite, Chl: chlorite, Chr: chromite, P-Chr: porous chromite, Orc: orcelite.

of Sb (up to 11 wt%). The structural formula varies from $(Ni_{11.38}Fe_{0.14})_{11.52}As_{6.32}Sb_{1.16}$ to $(Ni_{11.56}Fe_{0.14})_{11.70}As_{6.15}Sb_{1.14}$.

4.2. Chromitites of Lavanderos and Centinela Bajo Norte

4.2.1. Microstructure of the chromitite ores

The chromitites selected for this study come from the two shear zones of Centinela Bajo Norte and from the Lavanderos bodies (Fig. 2). They are massive chromitites that comprise >90 vol% chromite grains enclosed in an antigorite ± chlorite groundmass. These chromitites exhibit coarse-grained porphyroclasts of chromite up to 5 mm in diameter with cataclastic textures characterized by a dense network of fractures often filled by secondary chlorite (Fig. 3c). In samples with higher degrees of deformation the chromite grains are flat and show preferential orientation parallel to the shearing direction, which gives a local crude layering of chromite and antigorite ± chlorite (Fig. 3d).

Electron Back-Scattered Diffraction (EBSD) maps on selected areas of the studied samples containing PGM and/or BMM (Figs. 6a–f) show that chromite grains developed intracrystalline and intercrystalline fractures during deformation (Fig. 6a, c). This orientation mapping also allows identification of continuous crystallographic bending by crystal-plastic deformation before fracturing (Fig. 6b).

Energy dispersive spectrometry (EDS) maps show that chromite grains with an average misorientation per grain of ≤2° (Type A chromite: grains A1 and A2 in Fig. 6c, d) show two chemically distinct zones: (i) a relatively homogenous core enriched in Al (Fig. 6e) that forms the central part of the grain (dark area with slight misorientations in Fig. 6f), and (ii) a chemically distinct porous rim (Fig. 6e) with abundant silicate inclusions (outer part, light area with higher misorientations in Fig. 6f). The latter chromite is classified microstructurally as *partly altered chromite* (Gervilla et al., 2012; Barra et al., 2014). In contrast, grains with higher degrees of misorientation (2–8°) have relatively homogeneous chemical composition across the entire grain (Type B chromite: grains B1 and B2 in Fig. 6d). Quantitative analyses on these grains using electron microprobe (see following section) show the typical Fe^{2+}-rich and Mg- and Al-poor composition and spongy texture of *porous chromite* (Gervilla et al., 2012; Barra et al., 2014).

The correlation between the degree of misorientation (deformation) and higher degrees of alteration in chromite (i.e., formation of secondary Fe^{2+}-rich porous chromite) is more clearly seen near the fracture cross-cutting the Type A grain shown in Fig. 6e–f. Here, significantly higher degrees of misorientation (1–5°) are associated with the lowest Al contents.

4.2.2. Major element composition of chromite

In-situ EMPA and LA-ICPMS analyses were carried out across selected grains of chromite hosting inclusions of PGM ± BMM ± chlorite. The data are plotted in Fig. 7a–f and listed in Appendix 2 and Appendix 3.

The cores of Type A chromite grains at Centinela Bajo Norte show compositions of major elements that vary from 48.7 to 53.4 wt% Cr_2O_3, 16.4 to 19.8 wt% Al_2O_3, 1.5 to 3.3 Fe_2O_3, 12.1 to 14.9 wt% MgO, and 11.8 to 15.6 wt% FeO. The Cr# [Cr/(Cr + Al) atomic ratio] ranges

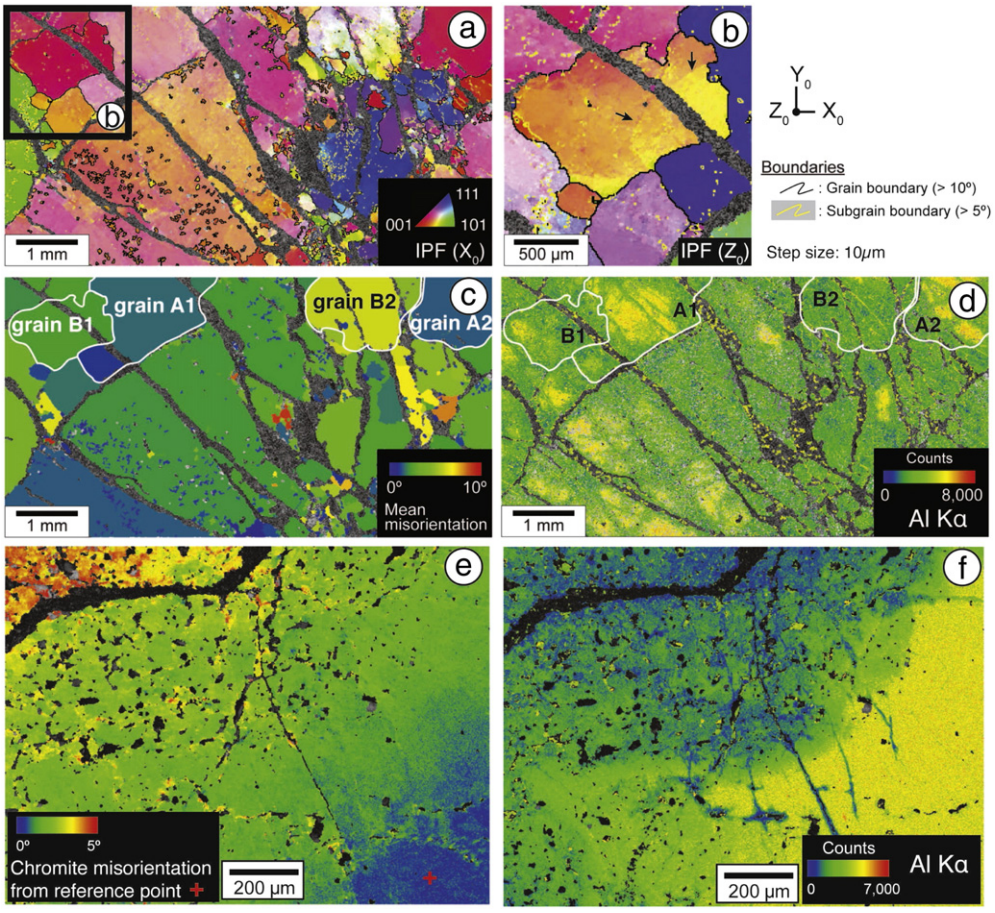

Fig. 6. EBSD and EDS maps of chromite grains exhibiting different representative microstructures of chromitites collected from Lavanderos. (a–b) EBSD map showing crystal orientation changes relative to the X_0 direction in (a) and Z_0 direction in (b). Black arrows in (b) represent the trace of crystal bending. (c) Color coded EBSD map depicting the mean orientation per grain. Thick white lines represent grain boundaries before fracturing. Step size is 10 µm. (d) EDS map of Al contents. Panels (e–f) show the rim of a single grain of partly altered chromite. (e) EDS map of Al contents. (f) EBSD map showing the change of orientation from a reference orientation (red cross) by maximum misorientation of 5°. Step size is 2 µm.

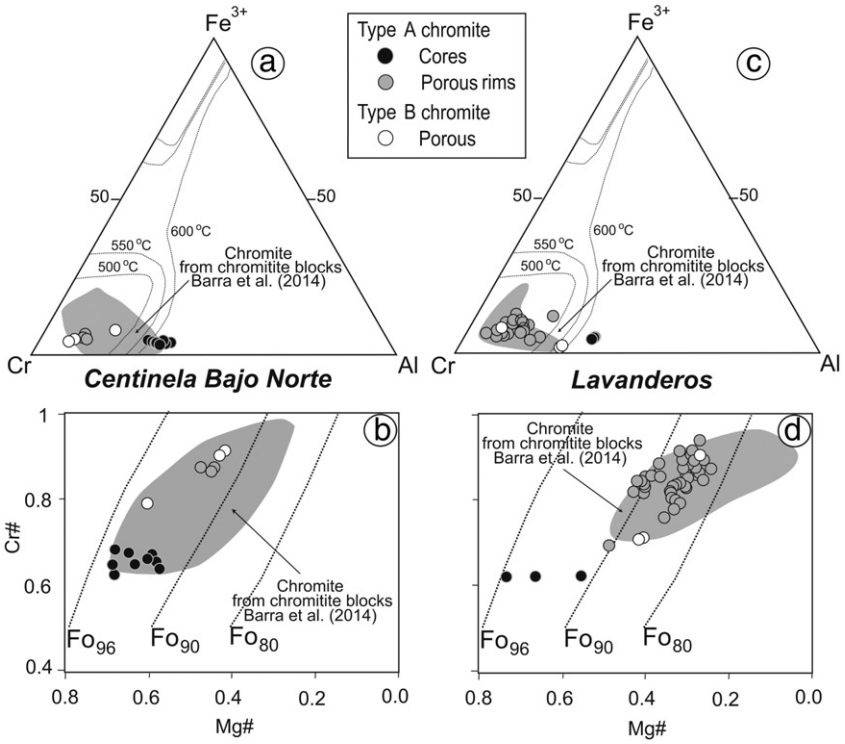

Fig. 7. Composition of chromite from La Cabaña chromitites analysed in this study. Data shown in plots (a–d) were obtained using EMPA, whereas those represented in plots e–f were obtained using EMPA (Al_2O_3, MgO, FeO^{tot}, Cr_2O_3) and LAC-ICMPS (Ga, Ti, Ni, Zn, Co, Mn, V, Sc). Shaded field in plots triangular plots (with chromite solvus shown at different temperatures by Sack and Ghiorso, 1991) in a–d are chromite compositions of La Cabaña chromitites reported by Barra et al. (2014), whereas in e–f correspond to the composition of unaltered chromite from the ophiolitic chromitites of Thetford Mines (Pagé and Barnes, 2009) and eastern Cuba (González-Jiménez et al., 2014b).

from 0.63 to 0.69, and the Mg# [$Mg/(Mg + Fe^{2+})$ atomic ratio] from 0.58 to 0.69; the $Fe^{3+}/(Fe^{3+} + Fe^{2+})$ atomic ratio ranges from 0.1 to 0.2 (Fig. 7a–b). The rims of porous chromite surrounding these cores show higher contents of Cr_2O_3 (56.4–63.6 wt%), total iron (Fe_2O_3 = 2.8–6 wt% and FeO = 11.8–15.6 wt%) but lower Al_2O_3 (3.9–9.8 wt%) and MgO (7.9–12.3 wt%). As is seen in Fig. 7b, this is reflected in higher Cr# (0.79–0.91) and lower Mg# (0.42–0.61), which are coupled with $Fe^{3+}/(Fe^{3+} + Fe^{2+})$ atomic ratios varying between 0.12 and 0.28 (Appendix 2). The Type B grains show very similar compositions to these porous rims with enrichment in Cr_2O_3 (60.9–61 wt%), total iron (Fe_2O_3 = 3.5–4.7 and FeO = 18.1–18.7 wt%) and depletion in Al_2O_3 (5.7–6.2 wt%) and MgO (8.3–9.2 wt%). These values correspond to Cr# = 0.87–0.88, Mg# = 0.45–0.48 and $Fe^{3+}/(Fe^{3+} + Fe^{2+})$ = 0.14–0.19 (Fig. 7a–b).

The Type A chromite grains from the Lavanderos chromitites show chemical trends of the major elements similar to their equivalents in Centinela Bajo Norte. Nevertheless, the former cores have slightly lower content of Cr_2O_3 (48.8–49.5 wt%) but higher Al_2O_3 (19.4–20 wt%) and total iron (Fe_2O_3 = 3.2–4 wt% and FeO = 10.4–16.7 wt%) and more variable MgO (11.7–16.1 wt%) (Fig. 7c). Thus, the cores of Type A grains of Lavanderos show a more restricted Cr# (0.62–0.63) but wider Mg# (0.55–0.73) and higher $Fe^{3+}/(Fe^{3+} + Fe^{2+})$ atomic ratios (0.15–0.26) than the cores of Type A grains from Centinela Bajo Norte (Fig. 7d). The rims surrounding Type A cores at Lavanderos also have significantly higher Cr_2O_3 (53.1–58.8 wt%) and FeO (19.9–22.7 wt%) with lower Al_2O_3 (4.2–14.5 wt%) and MgO (4.7–7.9 wt%), which corresponds to Cr# = 0.7–0.9, Mg# = 0.3–0.4 and $Fe^{3+}/(Fe^{3+} + Fe^{2+})$ = 0.1–0.2 (Fig. 7d). Similarly to Centinela Bajo Norte, the Type B chromites at Lavanderos are compositionally similar to the porous rims surrounding the cores of Type A chromites. These Type B chromites have Cr_2O_3 between 48.6 and 61.1 wt%, Al_2O_3 between 2.5 and 15.4 wt%, Fe_2O_3 between 2.6 and 9.6 wt%, FeO between 18.2 and 23.6 wt%, and MgO between 4.3 and 9.7 wt% (Fig. 7c). These values correspond to Cr# = 0.7–0.9, Mg# = 0.3–0.5 and $Fe^{3+}/(Fe^{3+} + Fe^{2+})$ = 0.12–0.3 (Fig. 7d).

All the analysed chromites plot within the compositional field defined by Barra et al. (2014) for chromites in chromitites in both localities (Fig. 7a–d). The chromites from the massive chromitites we have investigated in this study do not show ferrian chromite rims (i.e., Fe^{3+}-rich chromite), such as those described by these authors as surrounding some accessory chromite grains in the serpentinized dunites at Centinela Bajo Norte.

4.2.3. Trace element composition of chromite

In Fig. 7e–f the trace element composition of chromite from La Cabaña are plotted along unaltered high-Cr chromites from the ophiolites at Thetford Mines in Canada (Pagé and Barnes, 2009) and Sagua de Tanamo in Cuba (González-Jiménez et al., 2014b), all of which have been normalised to the composition of chromite from MORB (Pagé and Barnes, 2009).

The trace element abundances measured in the cores of Type A chromites from Centinela Bajo (thick black line) overlap that of the unaltered chromites from the ophiolites of Canada and Cuba. However, chromites from Centinela Bajo Norte are slightly depleted in Ni (<543 ppm), Zn (<413 ppm), Co (<218 ppm) and Mn (<1546 ppm), and slightly enriched in Ti (up to 1136.3 ppm) and V (up to 1470 ppm) (Fig. 7e and Appendix 3). In contrast, the porous rims of the Type A chromites from Centinela Bajo Norte are slightly depleted in all elements. Their MORB-normalised patterns are characterized by positive anomalies in Ti (<215 ppm) relative to Ga (<3.5 ppm on average) and Ni (<188. 4 ppm), a positive slope in the segment Zn–Co–Mn, and a strong depletion in V (<531.4 ppm) and Sc (<3.1 ppm). Type B chromites from Centinela Bajo Norte (i.e., porous chromite) show the overall lowest abundances of minor and trace elements (Fig. 7e and Appendix 3). They have similar patterns than the porous rims in the segment from Al_2O_3 to MgO and higher variability in Zn (from 44 to

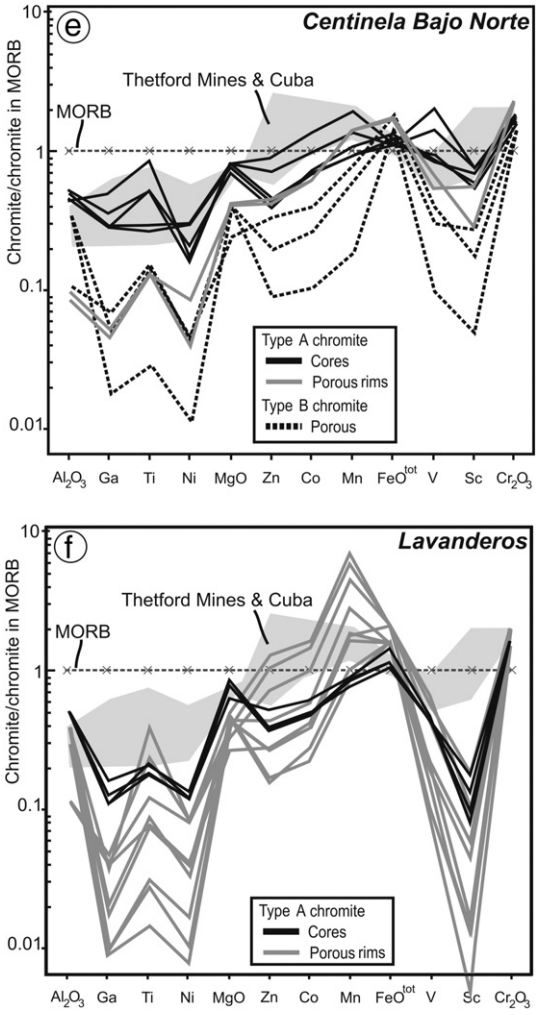

Fig. 7 (*continued*).

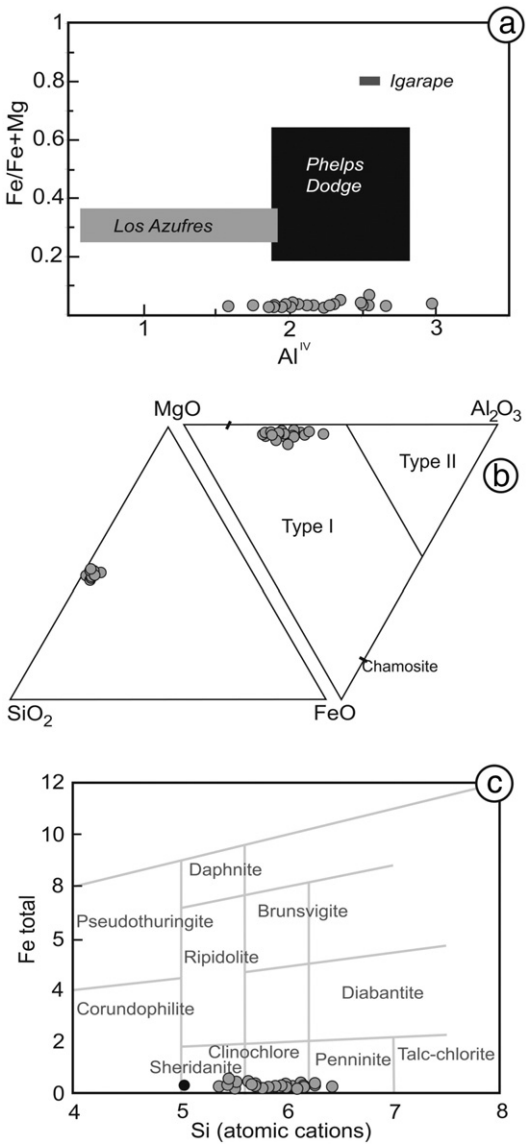

Fig. 8. Composition of the analysed chlorite filling pores of the secondary porous chromite in La Cabaña chromitites in terms of octahedral Al vs. tetrahedral Fe^{2+} and Mg^{2+} (a), SiO_2–FeO–MgO–Al_2O_3 with reference to type I and type II chlorites of Zane and Weiss (1998) (b), and Si vs. Fe total in the plot proposed by Hey (1954) (c). The fields shown in (a) correspond to those chlorites used for calibration of chlorite geothermometers in previous works from the literature, including Los Azufres (Cathelineau, 1988), Phelps Dodge (Kranidiotis and MacLean, 1987), Igarape (Zang and Fyfe, 1995).

167.8 ppm), Co (from 18 to 72.4 ppm), Mn (from 175.5 to 791.2 ppm), V (from 76 to 327 ppm), and Sc (<1.5 ppm).

The cores of Type A chromites from Lavanderos are distinctly different to those previously described at Centinela Bajo Norte. They plot between 0.1 and 1 times the normalising values, and outside the compositional field of chromites from the unaltered ophiolites of Canada and Cuba (Fig. 7f). These cores show a relatively flat trend from Al_2O_3 to MgO with a slight positive Ti anomaly (<295 ppm) relative to Ga (<8.9 ppm) and Ni (<248.4 ppm), and a remarkable negative anomaly in Sc (<1 ppm) (Fig. 7f and Appendix 3). Elemental patterns of the porous rims surrounding these cores plot between <0.01 and 10 times the chromite from MORB values and show the largest elemental variation. Like the porous chromite of rims of Type A chromite and the grains of Type B chromite in Centinela Bajo Norte, the porous rims at Lavanderos show a positive anomaly in Ti (<518.8 ppm) relative to Ga (<2.4 ppm) and Ni (<141.2 ppm), a positive slope in the segment Zn–Co–Mn, and strong depletion in V (<475.5 ppm) and Sc (<1 ppm) (Fig. 7f). Despite the similarity, there is a noticeable difference: porous rims at Lavanderos show much higher Zn (<581 ppm) and Co (<264.5 ppm) values and a pronounced positive Mn anomaly (up to 6265 ppm) (Fig. 7e–f and Appendix 3).

4.2.4. Chlorite composition

Chlorite grains are abundant in the porous rims of Type A chromite and everywhere in Type B chromite. Chlorite grains are intimately associated with pores in these chromites where they can be found as single isolated grains or ubiquitously associated with assemblages of PGM ± BMM.

The composition of chlorite determined by EMPA is characterized by large variations of SiO_2 but a very restricted range of $FeO_{(tot)}$, Al_2O_3, and MgO contents. In the diagrams shown in Fig. 8a–b the analysed chlorites plot on the Mg–Al joint. These Mg–Al chlorites correspond to Type I defined by Zane and Weiss (1998) based on the relations of Mg–Al–Fe (Fig. 8b). According to the conventional nomenclature based on the relation of Si content to Fe/(Fe + Mg) for chlorite, proposed by Hey (1954), most analysed grains of chlorite from the La Cabaña chromitites classify as sheridanite and clinochlore (Fig. 8c). Only three grains, which are associated with base-metal sulphides and arsenides, fall in the compositional field of penninite (Fig. 8c). One grain of chlorite associated with a PGM–BMM assemblage (irarsite + isoferroplatinum + stumpflite + orcelite) was analysed using EMPA and yielded a sheridanite composition (Fig. 8c). The relationship between chlorite composition and its parent (host) chromite is evidenced by their

relatively high Cr_2O_3 contents (from 2.30 to 8.1 wt%; 4.7 wt% on average; Appendix 4).

4.3. (PGE–Au) ± Ni–As–Sb–S mineralization in the chromitites

4.3.1. Bulk-rock contents of precious metals in the chromitites

Fig. 9 and Table 2 show the analyses of the precious metals (PGE–Au) for the La Cabaña chromitites. The PGE content in chromitites from both Centinela Bajo Norte and Lavanderos are generally uniform, ranging from 180 to 347 ppb (Table 2). The chromitites are distinctly enriched in the Ir-subgroup (Os + Ir + Ru = 166–305 ppb) compared to the Pt-subgroup (Pt + Pd + Rh = 14–43 ppb). PGE contents are between 0.002 and 0.1 times the chondritic values and show either irregular shapes with positive Ir anomalies relative to Os and Ru (i.e., Centinela Bajo Norte; Fig. 9a) or relatively flat patterns from Os to Ru, followed by strong negative slopes from Ru to Pd (i.e., Lavanderos; Fig. 9b). The PGE abundances and the general trends observed in Fig. 9 is similar to most Type-I chromitites found in the uppermost part of the mantle section of ophiolitic complexes (see González-Jiménez et al., 2014b). Gold is ubiquitous in the analysed chromitites, reaching up to 23.8 ppb in sample CAB-7B from Centinela Bajo Norte, the highest concentration reported so far in ophiolitic chromitites worldwide (e.g., Leblanc, 1991; Singh et al., 2013).

4.3.2. Mineralogy of precious metals

A total of 35 individual grains of PGMs and 9 of native Au (Au^0) were identified in 14 out of 55 polished thin sections investigated. These grains are distributed heterogeneously within a single thin section, and their mineralogy, chemistry and paragenetic relationships are reported in detail for the first time here (summarized in Figs.10a–z, 11a–c, Appendix 5 and Appendix 6). The grain size of PGMs and Au^0 is <10 μm in most cases, but a few grains are up to 30 μm in diameter. Thirty grains of PGMs were identified in the porous chromite as isolated inclusions or forming composite aggregates with other PGMs and/or BMM often intergrowth with secondary chlorite. The other five PGMs were observed embedded in the primary cores of Type A chromites. All grains of Au^0 were found associated with porous chromites in both fractures and pores filled with chlorite (Fig. 10u–w and Appendix 5).

The PGM population comprises specific minerals of all the six PGEs although there is a predominance of Os–Ir–Ru phases, consistent with the bulk-rock data. Among the identified mineral grains (Fig. 10a–z and Appendix 5), twelve are sulpharsenides of the irarsite–osarsite–ruarsite solid solution series (IrAsS–OsAsS–RuAsS), nine are Os-rich alloys, six laurites (RuS_2), and one is a Pt–Fe alloy. In addition, a series of PGE-bearing phases were only identified qualitatively by means of their EDS spectra, including five grains of an undefined RhS compound, two grains of PtSb (possibly stumpflite), one grain of Os–As (possibly omeiite; $OsAs_2$), and one grain of potarite (PdHg).

Table 2
Concentrations of precious metals in chromitite samples from the La Cabaña ultramafic bodies (in ppb).

Sample	Os	Ir	Ru	Rh	Pt	Pd	Au
Centinela Bajo Norte							
PODOB	22	157	126	12.9	28	2	0.5
CAB-7	29	93.3	136	7	19	10	0.5
CAB-7B	43	153	92	9.8	12	9	23.8
Lavanderos							
LA-C1	27	60.5	79	6.9	5	2	3.3
LA-C2	20	74.1	108	8.8	13	12	3.8
LA-C3	34	66	106	8.5	6	3	16.1

Irarsite is the most abundant PGM at La Cabaña (n = 7); it forms single isolated grains within pores of porous chromite or biphasic grains with laurite or osmium (e.g., Fig. 10g), as well as polyphase aggregates with Ni-rich sulphides and or arsenides (Fig. 10m, n and q). All these grains are always in contact with (or embedded in) secondary chlorite. In some cases, composite irarsite–laurite grains show partly corroded outlines (Fig. 10l and n). Overall, the analysed irarsite is characterized by very low contents of Os (<2.4 wt%) Ru (<1.76 wt%), and Rh (<0.99 wt%) (Fig. 11c; Table 3) and a significant depletion in As [As/(As + S) atomic ratio = 0.45–0.48]. This composition deviates from the ideal stoichiometry varying from $(Ir_{0.98}Ru_{0.03}Rh_{0.03}Fe_{0.02}Pt_{0.01})_{1.07}S_{1.02}As_{0.91}$ to $(Ir_{1.06}Rh_{0.02}Fe_{0.02})_{1.10}S_1As_{0.90}$. Unlike irarsite, osarsite contains appreciable amounts of Ru (up to 13.65 wt%) but a negligible Ir content (<0.86 wt%; Fig. 11c, Table 3) with a more variable As/(As + S) atomic ratio = 0.38–0.51. The structural formula ranges from $(Os_{0.48}Ni_{0.47}Ru_{0.14})_{1.09}S_{1.15}As_{0.71}$ to $(Os_{0.93}Ru_{0.07}Fe_{0.04}Ir_{0.01})_{1.06}S_{0.97}As_{0.96}$. The grain shown in Fig. 10i is internally heterogeneous due to S-deficiency as a result of partial desulfurization due to secondary alteration.

The second-most abundant PGMs are Os-rich alloys (Appendix 5). These grains are rarely larger than 10 μm across, and many of them are idiomorphic crystals associated with chlorite and located at the centre of radial cracks cutting primary cores of Type A chromite (Fig. 10a–d). Smaller grains of osmium can also be rounded inclusions within osarsite (Fig. 10i) or associated with other PGM hosted in Ni-rich sulphides (Fig. 10l; Appendix 6), and/or arsenides (Fig. 10n) filling pores of porous chromite. EMPA analysis of ~5μm² areas on the larger grains yielded the following compositional ranges (n = 12): 43.1–96.4 wt% Os, bdl–41.3 wt% Ir, 0.12–14.1 wt% Ru and up to 2 wt% Pt

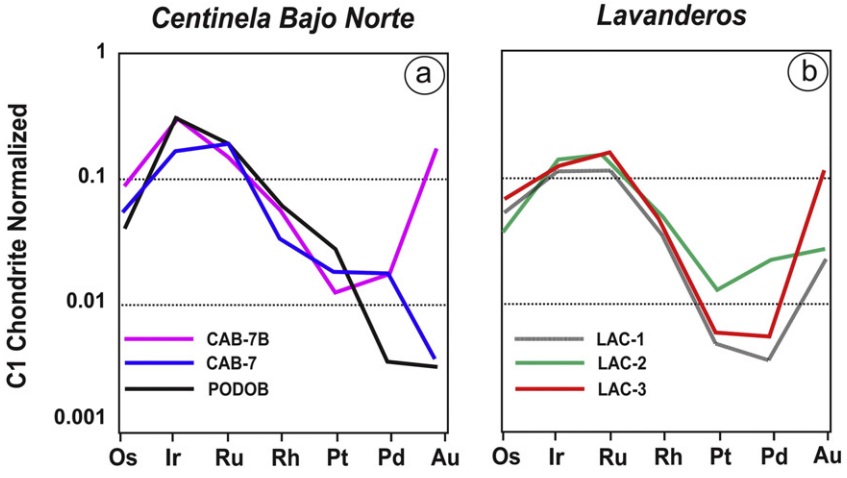

Fig. 9. Chondrite-normalised patterns (Naldrett and Duke, 1980) for precious metals in the two studied chromitite sites. Concentrations of platinum-group elements from González-Jiménez et al. (2014a).

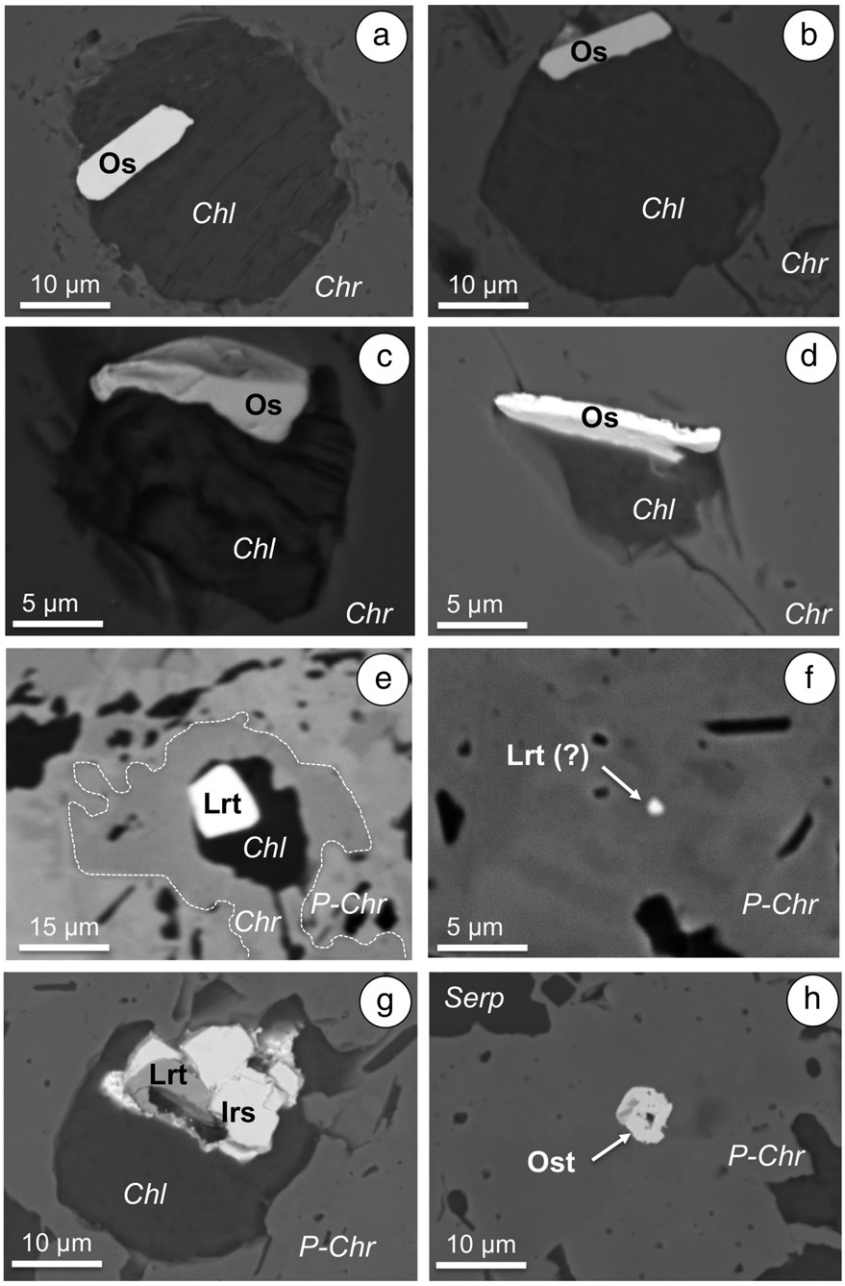

Fig. 10. Backscattered electron images of platinum-group minerals, gold and associated base-metal minerals found in La Cabaña chromitites. (a–e) Grains included in unaltered cores of chromite, (f–z) grains included in porous chromite or cracks cutting the chromite grains. Abbreviations: Bi: bismuth, Chl: chlorite, Chr: chromnite, Gdf: gersdorffite, Irs: irarsite, Lrt: laurite, Mil: millerite, Omt: omeiite, Orc: orcelite, Os: osmium, Ost: osarsite, P-Chr: porous chromite, Pdy: polydymite, Po: potarite, Serp: serpentine, Au: gold.

with no S (Table 3). In the Os–Ir–Ru plot these compositions fall in the field of osmium (Fig. 11a) but one of the analysed grains is osmium sensu stricto (i.e., Os^0) with no concentration of the PGEs except osmium (i.e., analysis #19 in Table 3). The remaining grains have appreciable amounts of Ir and Ru, yielding a structural formula that varies between $Os_{0.40}Ir_{0.37}Ru_{0.23}$ and $Os_{0.45}Ir_{0.33}Ru_{0.21}$.

Compositional profiles along single laurite grains present either as single isolated inclusions (e.g., Fig. 10e) or in composite aggregates with other PGM and/or BMM (Fig. 10g) show no core-to-rim chemical variations (Fig. 11b). The estimated composition for the analysed laurites (n = 6; Table 3) is nearly stoichiometric varying from $(Ru_{0.97}Ir_{0.03}Os_{0.02}Fe_{0.01})_{1.03}(S_{1.92}As_{0.05})_{1.97}$ to $(Ru_{0.99}Ir_{0.02}Fe_{0.01})_{1.02}(S_{1.93}As_{0.05})_{1.98}$.

The Pt–Fe alloy identified is intergrown with laurite and both are partly resorbed by a Ni-arsenide in contact with chlorite from the porous chromite (Fig. 10o). Quantitative analysis of this Pt–Fe crystal (n = 4; Table 3) reveals that it consists mostly of Pt (85.74–86.29 wt%) and Fe (11.31–11.69 wt%), with minor Ni (6.04–6.47 wt%) and Cu (6.93–7.20 wt%). The composition of this Pt–Fe alloy deviates slightly from an isoferroplatinum-type stoichiometry (Pt_3Fe), due to the appreciable amounts of Fe, Ni and Cu. Hereafter, we will refer to this phase as "Pt–Fe alloy" for the sake of convenience.

The other PGMs identified in the studied chromitites, that were identified qualitatively by their EDS spectra (including the RhS, PtSb, Os–As, Ir–Ni–(Ru) and Pd–Hg compounds) were found filling pores within the porous chromite either as single grains or forming composite grains with other PGMs or BMM (Fig. 10k, p, s, t and z). Similarly, native bismuth and gold grains were found in pores of porous chromite (Fig. 10u–y).

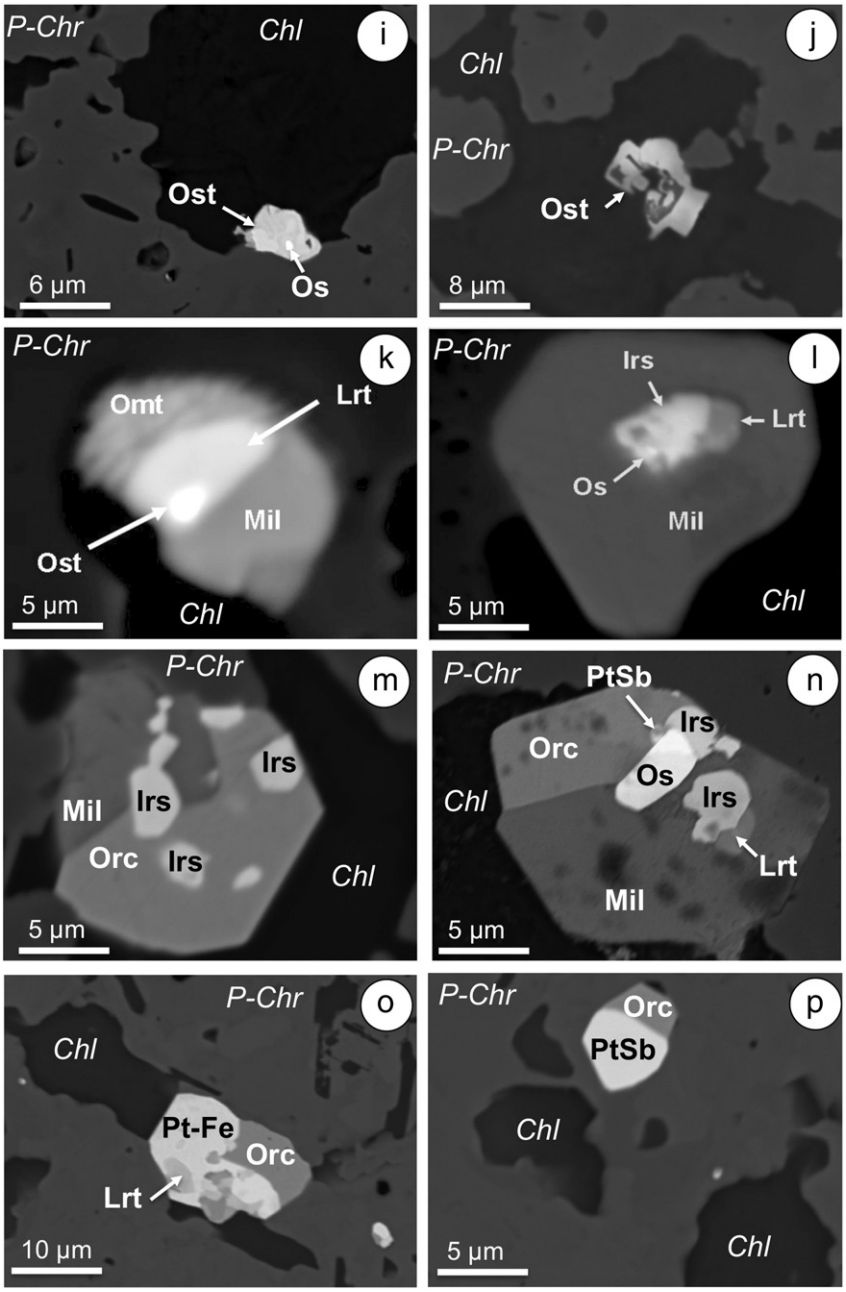

Fig. 10 (*continued*).

4.4. Base metal minerals

In addition to PGMs (Fig. 10k–p), grains of base-metal minerals (BMM) with sizes <80 μm were also observed within pores of the porous chromite (Fig. 12a–h). The following groups of BMM were identified (1) Ni–Fe–Cu sulphides, represented by millerite (NiS), polydymite (Ni_3S_4), violarite ($FeNi_2S_4$) and chalcocite (CuS); (2) Pb–Zn sulphides represented by galena (PbS) and sphalerite (ZnS); (3) Ni sulpharsenides represented by gersdorffite (NiAsS); and (4) the Ni arsenide orcelite ($Ni_{5-x}As$).

Millerite is the most abundant BMM and was detected in all the analysed samples. Some millerite grains are single-phase, but the majority are found as composite grains with polydymite and/or violarite (Fig. 12a–b). In these aggregates, polydymite and violarite occur within millerite cleavage planes and lamellar intergrown of polydymite and violarite are also common (Fig. 12c–f). Several of the grains made up of the assemblage millerite ± polydymite ± violarite are associated with gersdorffite and galena, which can be either intergrown with the Ni-sulphides (Fig. 12e–h). Additionally, element distribution maps suggest the presence of orcelite intergrown with millerite hosting PGMs (Fig. 10m–p; Appendix 6). Some other minerals found within chromite pores, which were identified only qualitatively by their EDS spectra, include two grains of sphalerite, chalcocite, and native bismuth (Bi^0).

Millerite analyses (n = 43) reveal a wide range of compositions, from nearly stoichiometric NiS (or $Ni_{1-x}S$) towards the more Fe-rich endmember $Fe_{1-x}S$ (Fig. 13; Appendix 7), with Ni ranging from 47.11 to 62.10 wt%, and Fe between 0.79 and 13.5 wt%. The structural formula varies from $(Ni_{0.98}Fe_{0.02})_{0.99}S_{1.01}$ to $(Ni_{0.73}Fe_{0.22})_{0.95}S_{1.05}$.

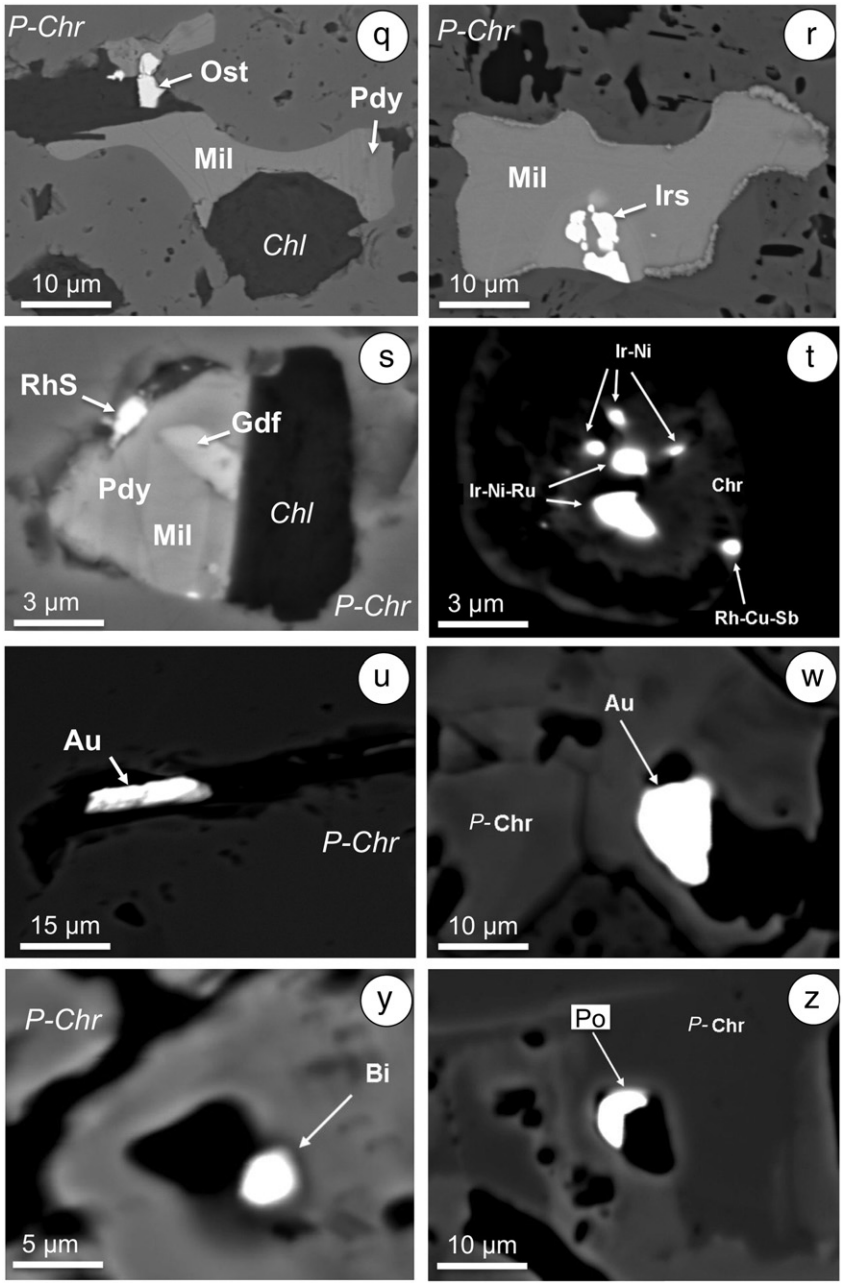

Fig. 10 (*continued*).

The analysed polydymite (n = 9) deviates from the ideal stoichiometry Ni_3S_4 (Fig. 13; Appendix 7) due to slight deficiency in S and elevated Fe content (up to 3 wt%). The average chemical formula of polydymite is $(Ni_{2.97}Fe_{0.11})_{3.08}S_{3.92}$.

The analyses of three large grains of violarite show Ni contents of 34.47–42.35 wt% and Fe contents of 12.82–18.76 wt% (Fig. 13; Appendix 7), with a corresponding formula of $Fe_{0.93}Ni_{2.02}S_{4.05}$.

Gersdorffite is more or less homogenous in composition (Fig. 13; Appendix 7); limited amounts of Co (6.17 wt%) and Fe (2.3 wt%) substitute for Ni (Fig. 13). The average formula obtained from the analysed grains (n = 24) is $(Ni_{0.94}Co_{0.07})As_{0.87}S_{1.12}$.

Galena is the only Pb-rich mineral in the studied chromitites. Its chemical composition is very homogenous, containing about 81–86 wt% Pb, up to 2.65 wt% Ni, and <1.5 wt% Fe (Appendix 7). The analyses of 12 grains give an average chemical formula of $Pb_{0.96}S_{0.97}$.

5. Discussion

5.1. Rheological conditions for chromite alteration: Insights from the linkage between microstructure and chemical variability

The EBSD maps of chromite show that chromitites at La Cabaña display similar deformational features that are disrupted by fractures (Fig. 6a–d). This implies that the now-unsupported fragments in the analysed samples were originally part of the same grain, suggesting the formation of subgrain boundaries and crystallographic bending before fracturing (Fig. 6b). These observations suggest that deformation started in a predominantly ductile regime with crystal-plastic deformation processes, which was later overprinted by brittle deformation. Interestingly, these crystallographic features produced by plastic deformation match with chemical variations measured in the chromite

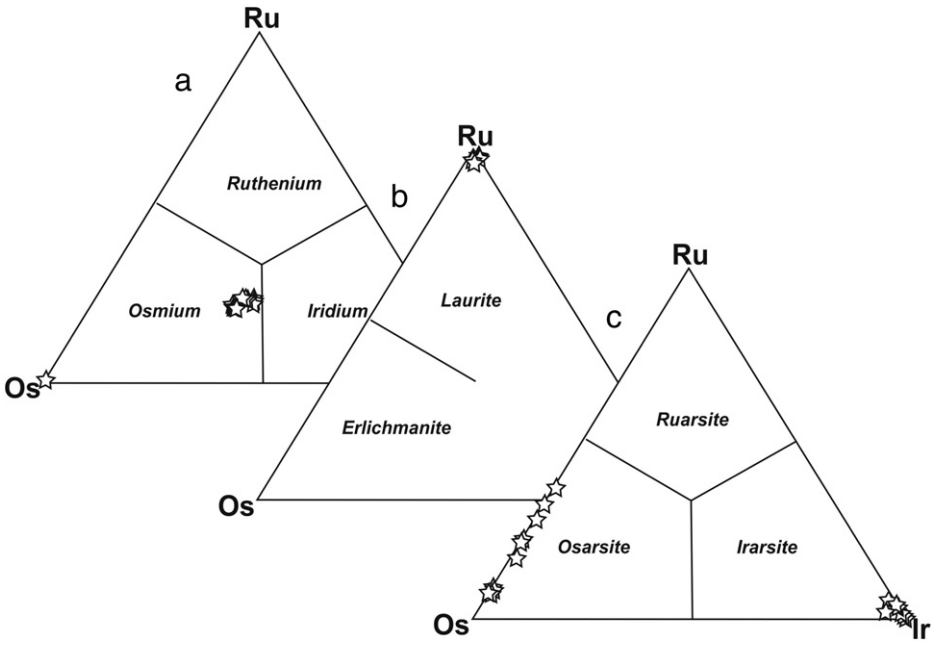

Fig. 11. Platinum-group mineral compositions of Ru–Os–Ir inclusions from La Cabaña chromitites. (a) Alloys, (b) sulphides of the laurite (RuS_2)–erlichmanite (OsS_2) series, (c) sulpharsenides of the osarsite (OsAsS)–ruarsite (RuAsS)–irarsite (IrAsS) series.

grains. Thus, in Type A chromite grains the cores are not deformed with no evidence of misorientation or subgrain boundaries (Fig. 6e–f) and almost preserve the magmatic signature in terms of major, minor and trace elements (Fig. 7e). These undeformed cores show low Cr# and high Mg# in equilibrium with igneous olivine ($Fo_{90–96}$; González-Jiménez et al., 2014a) (Fig. 6b–d), and in Centinela Bajo Norte the chromite grains display trace element signatures that overlap the compositional field of high-Cr chromites from unaltered ophiolitic chromitites (Fig. 7e). Therefore, our observations suggest that these domains correspond to relicts of primary igneous chromite grains unaffected by alteration.

In contrast, porous rims in Type A grains show progressively higher Fe^{2+}, lower Mg and Al, and depletion in all minor and trace elements (up to one order of magnitude for Ga, Ti and Ni; Fig. 7e) towards the edges of the grains. This chemical variation correlates spatially with a continuous crystallographic bending, as recorded by increasingly higher cumulative misorientation degrees (Fig. 6e–f). Such spatial correlation suggests that chemical modification was more effective along grain interfaces where the stress related with deformation was preferentially accommodated (e.g., Hull and Rimmer, 1959; Montagnat et al., 2011; Svahnberg and Piazolo, 2012, and references therein). Higher rates of crystal-plastic deformation would have promoted the formation and migration of dislocations, which would evolve into subgrain boundaries along the edges of the primary chromite grains (see grain A1 in Fig. 6b; Urai et al., 1986; Drury and Urai, 1990; Stipp et al., 2002). We suggest that these dislocations and subgrain boundaries would serve as pathways for the infiltration of external fluids and/or solid-state diffusion. Ongoing deformation would promote progressive crystal bending,

Table 3
Representative composition of platinum-group elements in chromitite samples from the La Cabaña ultramafic bodies. 1–3: laurite, 4–5: osarsite, 6–11: irarsite, 12–19: Os–Ir alloys, 20–22: Pt–Fe alloy.

Analysis wt%	Os	Ir	Ru	Pt	Pd	Rh	Fe	Ni	Cu	Co	S	As	Total	Os apfu	Ir apfu	Ru apfu	Pt apfu	Rh apfu	Fe apfu	Ni apfu	Cu apf	S apfu	As apfu
1	0.04	2.83	59.31	0.47	0.08	0.00	0.19	0.02	0.02	0.05	36.79	2.15	101.96	0.00	0.02	0.99	0.00	0.00	0.01	0.00		1.93	0.05
2	1.83	2.34	58.45	0.38	0.39	0.04	0.20	0.00	0.01	0.00	36.14	1.90	101.67	0.02	0.02	0.99	0.00	0.00	0.01	0.00		1.92	0.04
3	0.00	3.40	58.43	0.40	0.06	0.02	0.22	0.02	0.02	0.00	36.18	2.34	101.09	0.00	0.03	0.98	0.00	0.00	0.01	0.00		1.92	0.05
4	52.31	0.85	5.95	0.07	0.25	0.00	1.01	1.20	0.03	0.28	11.32	25.43	98.70	0.77	0.01	0.17	0.00	0.00	0.05	0.06		0.99	0.95
5	39.29	0.14	6.13	0.00	0.20	0.08	1.06	11.84	0.04	0.16	15.99	23.08	98.01	0.48	0.00	0.14	0.00	0.00	0.04	0.47		1.15	0.71
6	0.00	65.89	0.55	0.00	0.08	0.88	0.24	0.03	0.00	0.02	10.59	22.47	100.75	0.00	1.04	0.02	0.00	0.03	0.01	0.00		1.00	0.91
7	0.00	66.78	0.10	0.00	0.25	0.54	0.26	0.00	0.00	0.01	10.83	22.33	101.10	0.00	1.05	0.00	0.00	0.02	0.01	0.00		1.02	0.90
8	0.00	62.81	1.07	0.94	0.19	0.99	0.30	0.01	0.00	0.02	10.90	22.70	99.94	0.00	0.98	0.03	0.01	0.03	0.02	0.00		1.02	0.91
9	0.16	65.58	0.47	0.00	0.00	0.77	0.36	0.03	0.00	0.00	10.70	22.38	100.46	0.00	1.03	0.01	0.00	0.02	0.02	0.00		1.01	0.90
10	0.00	67.36	0.00	0.00	0.03	0.71	0.29	0.00	0.00	0.00	10.57	22.17	101.12	0.00	1.06	0.00	0.00	0.02	0.02	0.00		1.00	0.90
11	0.00	66.92	0.19	0.00	0.28	0.64	0.31	0.01	0.00	0.06	10.72	22.12	101.24	0.00	1.05	0.01	0.00	0.02	0.02	0.00		1.01	0.89
12	45.38	38.38	13.86	1.25	0.00	0.87	0.56	0.11	0.00	0.01	0.00	0.35	100.78	0.41	0.35	0.24							
13	44.96	38.03	13.67	1.45	0.23	0.52	0.58	0.09	0.00	0.02	0.00	0.31	99.86	0.42	0.35	0.24							
14	43.10	40.81	13.33	1.44	0.00	0.60	0.57	0.03	0.02	0.05	0.00	0.34	100.29	0.40	0.37	0.23							
15	43.85	41.29	13.21	1.91	0.00	0.74	0.49	0.07	0.00	0.00	0.00	0.38	101.94	0.40	0.37	0.23							
16	43.83	41.13	14.09	1.14	0.00	0.80	0.54	0.08	0.00	0.01	0.00	0.30	101.90	0.39	0.37	0.24							
17	48.93	37.02	12.31	1.65	0.00	0.42	0.48	0.06	0.00	0.00	0.00	0.01	100.89	0.45	0.34	0.21							
18	49.40	35.90	12.46	1.38	0.15	0.45	0.45	0.00	0.00	0.01	0.00	0.00	100.21	0.46	0.33	0.22							
19	96.36	0.00	0.12	0.00	0.07	0.00	0.36	2.88	0.06	0.01	0.06	0.00	99.91	1.00	0.00	0.00							
20	0.17	0.00	0.10	77.31	0.00	0.26	10.20	5.45	6.49	0.00	0.05	0.35	100.37				2.05		0.94	0.48	0.53		
21	0.17	0.00	0.07	78.81	0.00	0.40	10.54	5.72	6.13	0.00	0.03	0.00	101.87				2.05		0.96	0.50	0.49		
22	0.00	0.00	0.00	78.64	0.00	0.23	10.66	5.90	6.32	0.02	0.07	0.03	101.86				2.03		0.96	0.51	0.50		

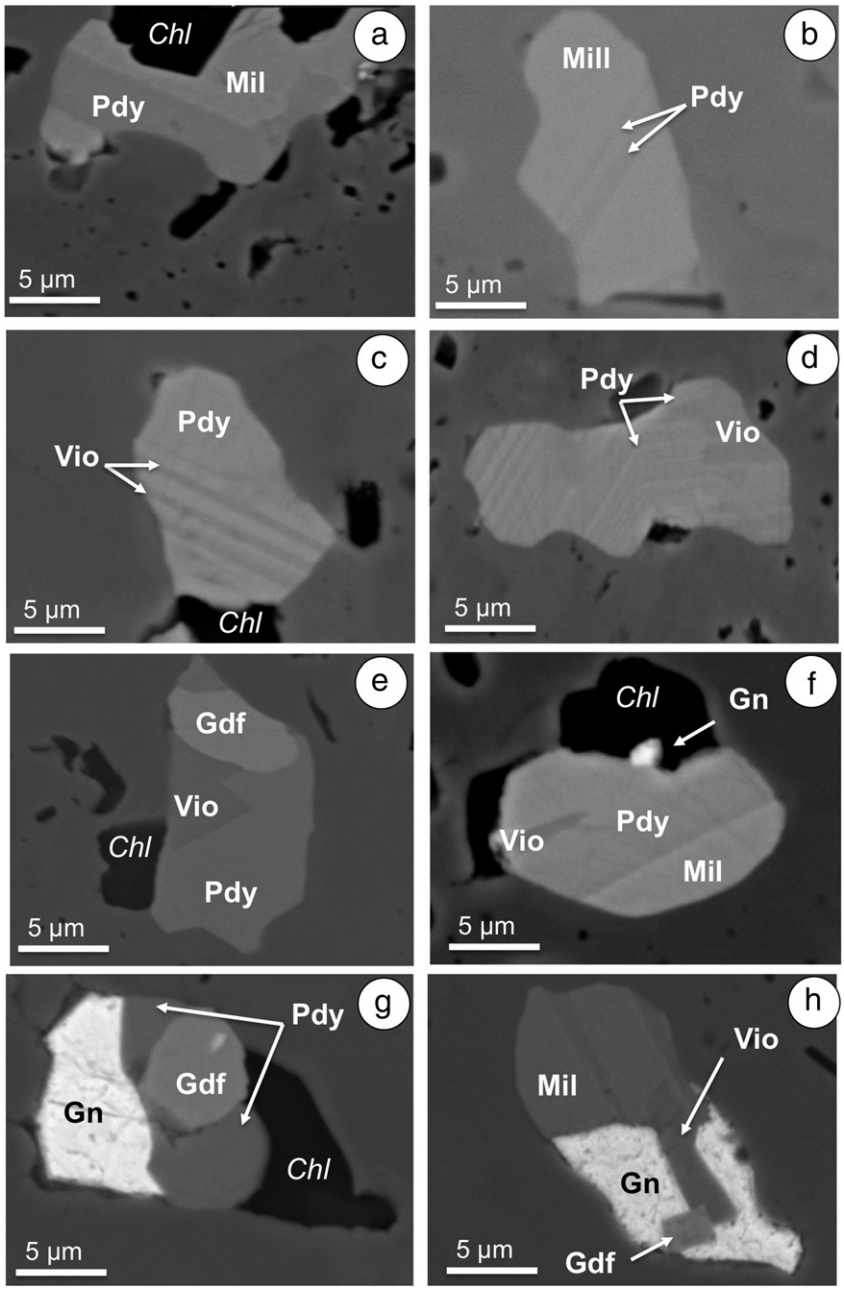

Fig. 12. Backscattered electron images of base-metal minerals inclusions in porous chromite of the La Cabaña chromitites. Abbreviations: Chl: chlorite, Mil: millerite (NiS), Gdf: gersdorffite, Gn: galena, Pdy: polydymite, Vio: violarite.

producing the formation of several subgrain boundaries that would facilitate fluid infiltration and/or elemental mobility. This could explain why domains with the greatest degrees of misorientation per grain are the most chemically modified (e.g., rim of grain A1 and the complexly deformed grain B1; Fig. 6a, b and d).

The plastic deformation features of chromite have been ascribed to either mantle flow (Christiansen, 1986; Ghosh et al., 2013, 2014) or metamorphism (Ghosh and Konar, 2012; Satsukawa et al., 2015). Although some deformed chromites from unaltered ophiolite complexes seem to preserve evidence of high-T crystal-plastic deformation in the mantle, not every chromitite body that has been subjected to such conditions displays microstructures of deformation. For example, nodular chromites from the mantle section of the unaltered ophiolite of Vourinos analysed by Prichard et al. (2015) using the EBSD technique do not show microstructures related to deformation. Rather they preserve intact magmatic growth features which suggest that there is good chance for the preservation of undeformed domains in chromitite subjected to deformation, as deformation is mainly localized within the silicate-rich portions (Cassard et al., 1981; Christiansen, 1986). Although the presence of abundant grains of chlorite in the highly deformed domains of porous chromite (Fig. 6a–f) suggest that alteration was related with the infiltration of external fluids during deformation, the possibility that the La Cabaña chromites were deformed within the mantle cannot be completely ruled out.

Barra et al. (2014) interpreted chlorite present in the porous chromite of La Cabaña as precipitated from the metamorphic fluids that have caused the alteration of the chromite. According to these authors external fluids promoted the reaction of chromite with the olivine matrix, producing partial to complete replacement of original grains of chromite by secondary Fe^{2+}-rich porous chromite in equilibrium with chlorite. This replacement reaction involved dissolution and precipitation with continuous mass loss, which results in the development of

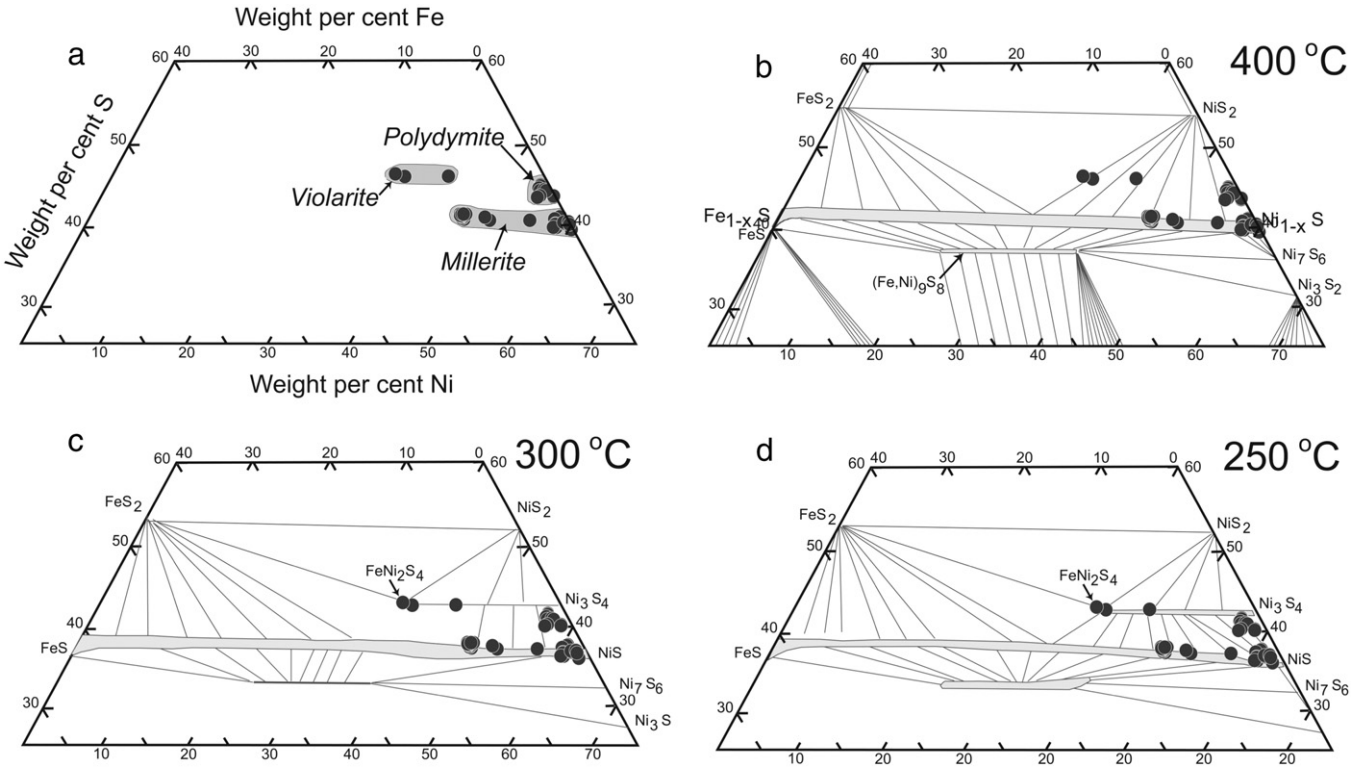

Fig. 13. (a) Composition of the analysed sulphides from the La Cabaña chromitites in the central portion of the ternary Fe–Ni–S system. (b–d) Mineral stabilities in the ternary diagrams of the analysed sulphides showing different mineral equilibria at 400 °C (b), 300 °C (c) and 250 °C (d) (Craig, 1973).

the porosity in chromite (Gervilla et al., 2012). During this event of dissolution–precipitation some small chromite grains could have been preserved amidst the dissolution, being rotated as a rigid bodies in a more ductile matrix made up of pores filled by fluid or chlorite. This can explain why some rims show slight misorientation relative to their cores (e.g., Fig. 6f) as well as the preservation of the observed microstructures of deformation despite the dissolution–precipitation processes.

If such replacement occurred under a fluid-assisted high-strain regime at relatively high-temperature conditions, the deformation in chromite should be accommodated by grain size reduction and/or re-crystallisation of the small insolated chromite grains. However, the formation of new small chromite grains (i.e., recovery textures), which usually involves the removal of the newly formed silicates in the most deformed grain, is not only associated with high strain but it also requires relatively high temperature conditions (>500–700 °C; Christiansen, 1986; Graham et al., 1996; Ghosh and Konar, 2012; Ghosh et al., 2013; Satsukawa et al., 2015). According to our estimates below, the alteration of chromite at La Cabaña took place at ~510–560 °C, which suggests that the lack of these features in chromitites should be related with deformation at lower strains than reported in other deformed chromitites around the world (e.g., Ghosh and Konar, 2012; Ghosh et al., 2013; Satsukawa et al., 2015). We suggest that once antigorite-bearing serpentinites started to form, soon after the fluid infiltration that produced the alteration of chromite, they preferentially accommodated most of the stress existing within the developing shear zone. The lubricating effect of the schistose serpentinite would suggest that chromite grains, if already deformed plastically, then behave as rigid bodies that rotate in a more ductile matrix, thus explaining the lack of recovery textures, as is typical of chromites deformed at moderately to high temperatures within shear zones (e.g., Satsukawa et al., 2015).

5.2. Temperature of chromite alteration

An independent method to estimate the temperature at which the alteration of chromite occurred is by determination of the phase equilibrium relations for the transformation of the assemblage chromite–olivine to Fe^{2+}-rich chromite–chlorite (Gervilla et al., 2012). In a previous work, Barra et al. (2014) analysed the phase relations in the system Cr_2O_3–MgO–Al_2O_3–SiO_2–H_2O (CrMASH) considering binary mixing between Cr and Al in the octahedral site of chromite and assuming water-saturated conditions. Using this thermodynamic approach these authors estimated a temperature of <500 °C for the formation of Fe^{2+}-rich chromite in the chromitites we have studied here. The results of their thermodynamic modelling suggest that during the formation of porous Fe^{2+}-rich chromite the variations of Cr# are nearly isobaric (particularly above 10 kbar) and that the gradient of variation in Cr# is strongly dependent on the volumetric chromite/olivine ratio of the rock. Therefore, pressure conditions for the alteration of chromite can hardly be estimated using this approach while the best record of the temperatures for alteration can be extracted using the composition of chromites from very massive chromitites.

Our refined model considers only the composition of chromite from massive chromitite but using a 1:1 molar mix of chromite:olivine in order to account the potential effect of the small size of the chromitite bodies in a larger volume of olivine-rich rock. Furthermore, we now consider all constituents of the system [i.e., Cr_2O_3–MgO–FeO–Al_2O_3–SiO_2–H_2O (CrMFASH)] since we have included the binary mixing between Mg and Fe^{2+} in the tetrahedral site of chromite (which is based on the ideal solution model proposed by Engi (1983). In this case, we have applied the thermodynamic approach using Perple_X (Connolly, 2009) with the expanded thermodynamic database of Holland and Powell (1998, revised 2002) to include Cr-bearing phases (cr_hp02ver.dat). The solid solutions considered here are the Cr-spinel (Klemme et al., 2009), olivine and chlorite (Holland and Powell,

1998). Other minerals involved in the calculations are pure phases (i.e., diaspore and brucite).

From this new modelling it can be seen that the porous chromite that formed at the maximum conditions for the metamorphic peak estimated for the rocks of the Western Series (i.e., ~420 °C and 9.3 kbar) should have Cr# = 0.94 and Mg# = 0.26 (yellow star-1 in Fig. 15b–c), whereas at the minimum conditions of retrograde metamorphism under greenschists-facies conditions it should have higher Cr# = 0.96 and lower Mg# = 0.21 (yellow star-2 in Fig. 15b–c). These values contrast with the composition of the porous chromite forming the massive chromitites from La Cabaña (including those from Centinela Bajo Norte and Lavanderos ultramafic bodies), which has a maximum Cr# = 0.9 and minimum Mg# = 0.3. These observations above suggest that the transformation of the assemblage chromite + olivine to Fe^{2+}-rich chromite + chlorite took place at temperature slightly higher than the metamorphic peaks estimated for the metasedimentary rocks that are spatially associated with the chromitite-bearing ultramafic rocks (Fig. 15b–c). Considering the uncertainty on pressure estimates due to the nearly isobaric nature of the reaction of chromite alteration, a simple calculation indicates alteration temperatures of 560 °C at 9.3 kbar (red circle-1 in Fig. 15b–c) and 510 °C at 3 kbar (red circle-2 in Fig. 15b–c). These temperatures are significantly higher than previously suggested by Barra et al. (2014) but consistent with those estimated for the formation of the metasomatic black-wall developed at the contact between serpentinites and host micaschists in Centinela Bajo Norte body (i.e., 520–550 °C; Höfer et al., 2001).

5.3. Chlorite geothermometry

The composition of chlorite hosted in the secondary porous chromite can be used as independent proxy to determine the alteration temperature. Several researchers have developed empirical geothermometers relating the chlorite composition to its formation temperature (Cathelineau and Nieva, 1985; Kranidiotis and MacLean, 1987; Zang and Fyfe, 1995; Shabani, 2009). These models are based on the variation in the tetrathedral Al content within chlorite, and have been calibrated against fluid inclusions microthermometric data in coexisting minerals. Cathelineau and Nieva (1985) noted that in the Los Azufres active geothermal system in Mexico there was a systematic increase in the Al^{IV} contents in chlorites with increasing temperature. They reached this conclusion by comparing the microtermometric data obtained from fluid inclusions hosted in gangue minerals in equilibrium with chlorite, and derived a formula from which the temperature in Celsius (T) can be estimated from Al^{IV} analysed in chlorite:

$$Al^{IV} = 4.71 \times 10^{-3}T - 8.26 \times 10^{-2}. \quad (1)$$

In a subsequent work Kranidiotis and MacLean (1987) applied the same approach but solved Cathelineau and Nieva's equation for T considering 8Si + Al^{IV}:

$$T = 106Al^{IV} + 18. \quad (2)$$

These authors included an additional correction for the value of Al^{IV}, as they concluded that Al measured in chlorite can potentially increase with increasing Fe/(Fe + Mg). The correction they applied was:

$$Al_{corrected}{}^{IV} = Al_{sample}{}^{IV} + 0.7Fe/(Fe + Mg). \quad (3)$$

Based on their work on the Igarapé Bahia gold deposit (Brazil), Zang and Fyfe (1995) rearranged this correction to the value at 0.34Fe / (Fe + Mg) proposing a distinct equation for the correction of the measured Al^{IV}:

$$Al_{corrected}{}^{IV} = Al_{sample}{}^{IV} - 0.88[Fe/(Fe + Mg) - 0.34]. \quad (4)$$

A more updated version of Cathelineau and Nieva's equation is presented by (Klein and Koppe, 2000; Shabani, 2009):

$$T = -61.92 + 321.98Al^{IV}. \quad (5)$$

Application of these equations to chlorite inclusions in porous chromite from the La Cabaña chromitites yields the flowing ranges of temperatures: [Eq. (1)] = 231–369 °C, [Eqs. (2) & (3)] = 188–336 °C, [Eqs. (2) & (4)] = 216–362 °C, and 262–430 °C [Eq. (5)] (Fig. 16; Appendix 4).

Although these geothermometers were developed for Al-rich chlorites precipitated from hydrothermal fluids in crustal settings, overall the computed temperatures for chlorite crystallisation in the La Cabaña chromitites overlap the window of temperature estimated from the host metasedimentary schists and associated rocks (Fig. 16). This suggests that the potential subsolidus Al–Fe re-equilibrium between chlorite and host chromite grains did not significantly impact the chlorite composition (e.g., Zane et al., 1998) and that these equations developed for chlorites from hydrothermal fluids in crustal domains can also be applied to our case study.

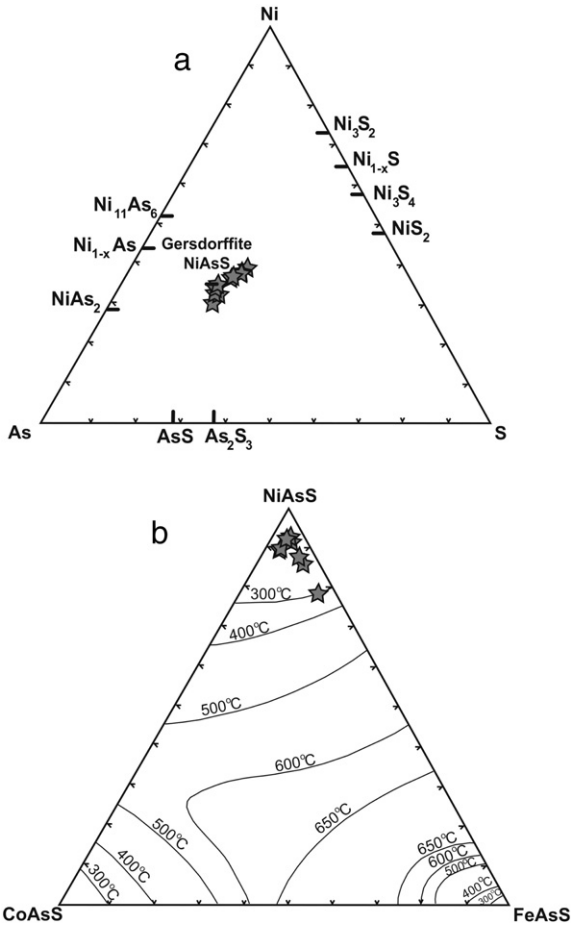

Fig. 14. (a) Composition of the analysed gersdorffite from the La Cabaña chromitites in the system NiAsS. (b) Plot of the analysed gersdorffite with references of the solvus in the condensed system CoAsS–NiAsS–FeAsS at 300 °C, 400 °C, 500 °C, 600 °C, and 650 °C (Klemm, 1965).

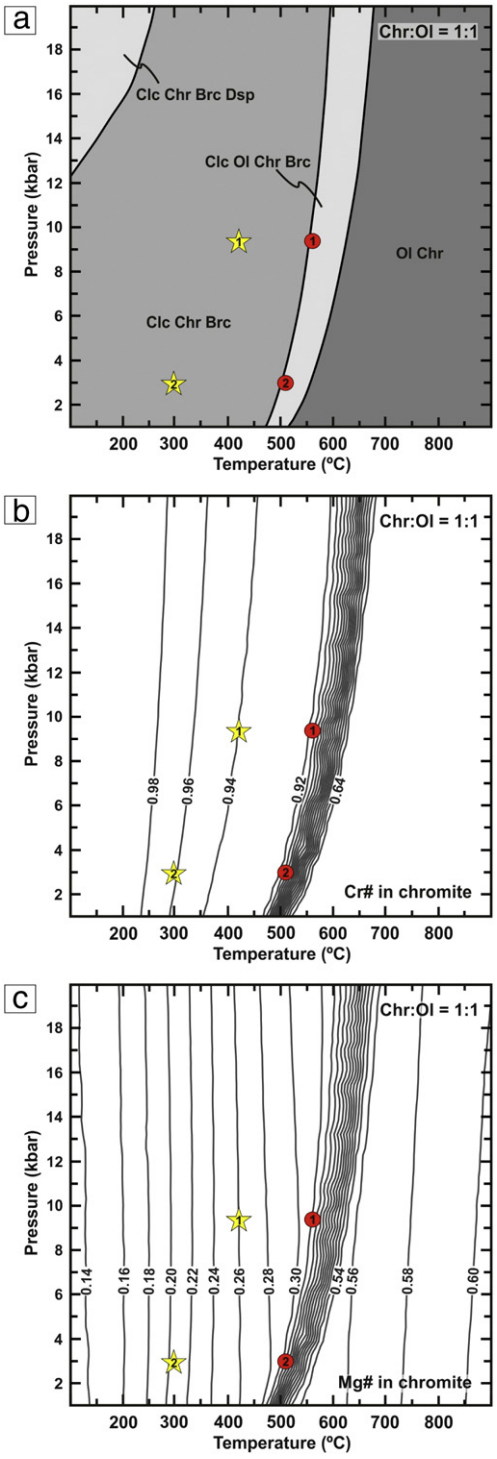

Fig. 15. (a) Isochemical phase diagram (pseudosection) calculated for a model chromitite composition in the CrMFASH system for 1:1 chromite:olivine molar proportions. Isopleths calculated for the same system and proportions of chromite:olivine are shown for Cr# and Mg# (mole proportion) in chromitites in (b) and (c) respectively. The yellow stars correspond to the predicted composition of the porous chromite at the maximum (i.e., ~420 °C and 9.3 kbar; yellow star-1) and minimum (~300 °C and 3.5 kbar; yellow star-2) PT conditions. The red circles indicate the composition of the analysed porous chromite in La Cabaña chromitites along an isopleth but at different pressures.

5.4. Phase relations in the system Ni–Fe–S–As

All identified Ni-rich sulphides, arsenides and sulpharsenides were found in pores (and chlorite filling these pores; Fig. 12a–h) of porous chromite, which clearly attests to their secondary origin, related to the metamorphism of the host chromite. The specific temperatures in which these secondary opaque minerals were formed can be estimated with some precision, using available experimental data and the Fe–Ni–S–As phase equilibrium relationships shown in Figs. 12a–h and 13.

The analysed millerite grains in the La Cabaña chromitites exhibits significant variation in the contents of Fe, from bdl up to 13.5 wt% (Fig. 13). According to the experimental results of Craig (1971, 1973) these Ni-deficient compositions of $Ni_{1-x}S$ are stable only below 400 °C where there is an extensive solid solution between $Fe_{1-x}S$ and $Ni_{1-x}S$ (Fig. 13). However, at 379 °C the high-temperature structure of the solid solution $\alpha Ni_{1-x}S$ inverts to the low temperature polymorph $Ni_{1-x}S$. This low-temperature polymorph has a maximum Fe content of 5 wt% and is stable down to 282 °C, below which it decomposes to form polydymite and millerite sensu stricto (Kullerud and Yund, 1962; Craig, 1973). A series of similar polymorphic transformations during the subsolidus re-equilibration in the Ni-rich region of a precursor low-temperature monsulphide solid solution (*mss*) can well explain the compositions determined for the La Cabaña millerites (Fig. 13) as well as the millerite–polydymite association observed in Fig. 12a–b; the later composite aggregates had to form at temperature ca. 282 °C and were fully equilibrated at 250 °C according to the tie-lines on the phase diagrams of Craig (1973) (Fig. 13).

On the other hand, a series of experimental results (Craig, 1971, 1973; Fleet, 2006) shows that violarite (ideally $FeNi_2S_4$) has complete solid solution with the end-member polydmite (Ni_3S_4) at 356 °C. Tie-lines on Ni–Fe–S phase diagram (Fig. 13) show that the violarite of the La Cabaña chromitite could be in equilibrium with polydymite at 300 °C, and seem to remain at this composition at least down to 250 °C (Fig. 13; Fleet, 2006). Again, this suggests that these sulphide assemblages would form at temperatures close to 300 °C and were fully equilibrated at much lower temperature.

The fact that in the two types of Ni-rich sulphide assemblages discussed above the different members show crystallographically oriented disposition and/or polysynthetic twins parallel to the prismatic planes (Fig. 12a–f) clearly suggests solid-state exsolution from a precursor low-temperature *mss*. Furthermore, the presence of single grains of nearly stoichiometric millerite suggests subsolidus re-equilibrium with the chromite host, whereby Fe is removed from the sulphides to fill vacancies in the chromite (Naldrett and Lehmann, 1988; Naldrett et al., 1989). Therefore, the precursor low-temperature *mss* had a higher Fe concentration than its products. This Fe-rich nature can explain the formation of violarite and polydymite in the Ni-deficient region of the low-temperature *mss*, similarly to what is observed in experiments (Craig, 1971, 1973; Fleet, 2006).

Another feature of the Ni-rich sulphide assemblages in the La Cabaña chromitite deserves further discussion: the intimate association of these minerals with the As-rich mineral gersdorffite (Fig. 12e, g and h). A possible explanation for the observed texture is the formation of gersdorffite with Ni-rich sulphides from the original low-temperature *mss* with significant amounts of As. The experimental results of Yund (1962) show that at >400 °C there is extensive solid solution between $Ni_{1-x}As$ and $\alpha Ni_{1-x}S$, and As and S in NiAsS, respectively. He also synthetized gersdorffite (NiAsS) co-existing with polydymite (Ni_3S_4)–millerite (NiS) at <356 °C. Below 280 °C, the solid solution NiAs–NiS decomposes into the assemblage gersdorffite (NiAsS) + $Ni_{1-x}S$ + rammelsbergite ($NiAs_2$) (Testafaye and Taskinen, 2010). These experimental data allow us to bracket the formation of the assemblage gersdorffite + Ni-rich sulphides between 356 and 280 °C. A formation temperature of ~300 °C is suggested for gersdorffite of the La Cabaña chromitite based on its low cobalt content (Fig. 14). The microstructural position of galena at the margins of the Ni-rich sulpharsenide + Ni-rich sulphide assemblage (Fig. 12g–h) suggests that it was exsolved later.

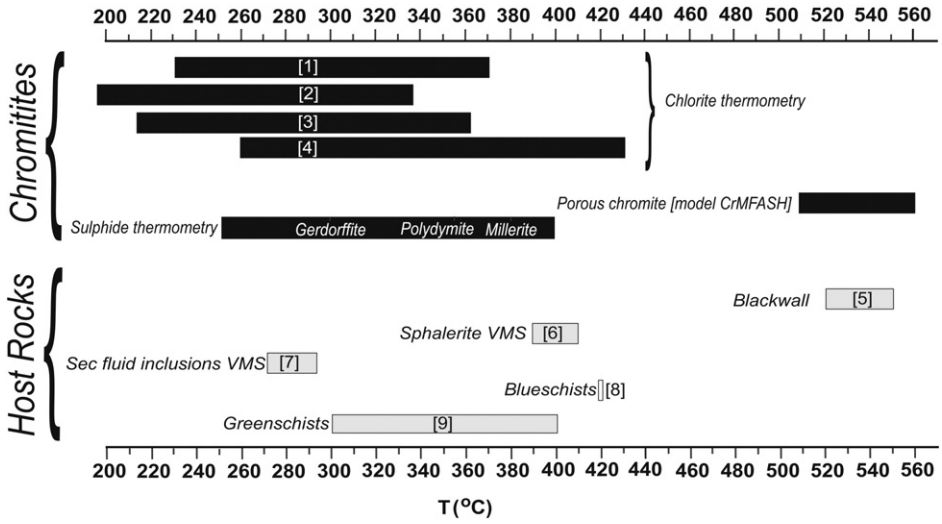

Fig. 16. Temperatures obtained from chlorite composition, chromite and sulphides analysed in this work. For comparison we have also included the temperatures estimated for metamorphic and associated VMS deposits neighbouring the La Cabaña ultramafic bodies. Numbers in brackets correspond to the following references: 1: Cathelineau and Nieva (1985), 2: Kranidiotis and MacLean (1987), 3: Zang and Fyfe (1995), 4: Klein and Koppe (2000), 5: Höfer et al. (2001), 6 and 7: Collao and Alfaro (2000), 8 and 9: Willner et al. (2001).

5.5. Origin of the (PGE–Au) ± Ni–As–Sb minerals

The population of precious metals includes phases of all six PGEs as well as native gold, although there is a clear predominance of Os, Ir and Ru minerals (Fig. 10a–z; Appendix 5). This precious metals mineralogical distribution is in good agreement with the chondrite-normalised PGE + Au patterns, indicating that PGMs and native gold are the main mineralogical hosts for the precious metals in the La Cabaña chromitites.

Most PGM grains were found in porous chromite associated with secondary chlorite, except a few grains of osmium that are included in unaltered cores (Fig. 10a–d). The shape of these alloys (e.g., Fig. 10a–b), and their lack of S rules out an origin derived from in situ desulfurization at low temperatures of a primary Os–Ir–Ru-bearing sulphide (e.g., Stockman and Hlava, 1984; Garuti and Zaccarini, 1997; Grieco et al., 2006; Proenza et al., 2008). Rather, these alloys must have formed at high temperature, before or during the crystallisation of chromite. A similar interpretation can be assumed for the grain of laurite occurring within chromite and in contact with an open fracture filled with chlorite (Fig. 10e). The fact that these PGMs are always associated with chlorite at the centre of radial crack systems is a clear indication that their formation predated brittle fracturing of the chromite host (e.g., Stockman and Hlava, 1984; Torres-Ruiz et al., 1996).

According to the experimental results of Brenan and Andrews (2001) and Andrews and Brenan (2002) laurite and Ru-poor Os–Ir alloys with compositions similar to those identified in the La Cabaña chromitite can crystallise directly from basaltic melts at 1200–1300 °C and log fS_2 from −2 to −1.3 (Melcher et al., 1997; Brenan and Andrews, 2001; Bockrath et al., 2004; Gervilla et al., 2005; Grieco et al., 2006; Barnes and Fiorentini, 2008; Finnigan et al., 2008; González-Jiménez et al., 2009). However, in natural systems both types of PGMs can also be formed, via sulphur removal, during progressive partial melting of peridotite-hosted PGE-rich BMS (Nakagawa and Franco, 1997; Peregoedova et al., 2004; Shi et al., 2007; Lorand et al., 2010; Fonseca et al., 2012). Once these PGMs are segregated they can mechanically trapped by growing chromite (González-Jiménez et al., 2009; Uysal et al., 2009). Both mechanisms can explain the significant variations in the $^{187}Os/^{188}Os$ ratios exhibited by the La Cabaña PGMs (González-Jiménez, unpublished data). Therefore, the PGMs shown in Fig. 10a–e are considered as primary minerals that were unaffected by the infiltrating metamorphic fluids that produced the metamorphic/porous chromite and the secondary chlorite.

The primary vs. secondary origin of the other PGMs found in porous chromite rims, commonly associated with silicates and/or Ni-rich sulphides and arsenides (Fig. 10f–t), is more difficult to interpret. Similar assemblages of PGMs (including abundant Os–Ir–Ru sulpharsenides, laurite, Pt-rich alloys and antimonides) associated with Ni-rich arsenides, sulpharsenides, bismuthides and antimonides, have been described in the unaltered chromitites of the Ojén Lherzolite Massif in southern Spain (Torres-Ruiz et al., 1996; Gervilla et al., 2002; Gutierrez-Narbona et al., 2003; González-Jiménez et al., 2013), and the altered chromite rims of chromitites from the strongly metamorphosed ophiolites of Shetland, Scotland (Prichard et al., 1994) and Bou-Azzer, Morocco (El Ghorfi et al., 2008).

In the Ojén lherzolite massif the abundance of As- and Sb-bearing minerals was related to the precipitation of chromitites from small-volume melts (Gervilla et al., 2002; Gutierrez-Narbona et al., 2003) enriched in volatiles and incompatible elements (i.e., As, S, Sb, Bi, PGE). Recently, Piña et al. (2015) have confirmed this hypothesis, showing that in these chromitites the sulphides contain appreciable quantities of As, Sb, and Bi. The injection of a chromite-bearing hydrous silicate fluid enriched in incompatible elements could explain the disrupting vein-like morphology of the Lavanderos chromitites as well as the presence in these chromite ores of Pt- and Sb-rich minerals (i.e., Pt–Fe alloys and Pt–Sb; Fig. 9o–p). Likewise, high aAs and fS_2 in the latest stages of evolution of the parental melt could also explain the formation of Ni-arsenide/sulphide assemblages associated with the PGMs observed in Fig. 9m–n (e.g., Gutierrez-Narbona et al., 2003). Although this possibility cannot be completely ruled out, the fact that most of these PGM + base-metal minerals fill the interstitial spaces of porous chromite – together with secondary chlorite – suggests that they were linked to, or at least affected by, the metamorphic overprinting event (e.g., Prichard et al., 1994; El Ghorfi et al., 2008).

Considering this second alternative, primary PGMs originally included in the chromite grains must have been liberated from their original positions by partial dissolution of the host and then interacted with post-magmatic solutions (e.g., Yang and Seccombe, 1993; Moreno et al., 1999; Proenza et al., 2008; El Ghorfi et al., 2008; Augé et al., 2012). This could explain the irregular grain edges of PGM grains shown in Fig. 9f–j. Eventually, these aqueous solutions could carry Ni, As, S, and Sb resorbing partly or completely the pre-existing PGMs. This would explain the textural disequilibrium between the PGMs (laurite and Os–Ir sulpharsenides) and host millerite in polyphase aggregates (Fig. 10k–l), and the biphasic grain of Pt–Fe alloy + laurite shown in Fig. 10o, where both PGMs were partially resorbed into the

Ni-arsenide. The internal relationships in the aggregates shown in Fig. 10m–n suggest the readjustment of this As–Ni–S–(Sb) solid solution through a series of polymorphic transitions during subsolidus cooling, thus producing the observed Ni-rich sulphide, arsenide and antimonide. During the polymorphic transition it is likely that PGE admixed to form discrete in situ *neoformed* PGMs (e.g., inclusions of irarsite in Fig. 9m), similarly to those observed in experiments and natural samples (Makovicky et al., 1986; Makovicky et al., 1988; Ballhaus and Ulmer, 1995; Peregoedova and Ohnenstetter, 2002).

The presence of PGMs at the margins of larger grains of millerite (e.g., Fig. 10q–r) or aggregates of millerite–polydymite–gersdorffite (Fig. 10s) associated with chlorite filling the chromite interstices, strongly suggests ex situ precipitation of PGM ± Ni-arsenides ± Ni-sulphides assemblages from a metamorphic fluid. Under such scenario, it is likely that PGE- and Ni–As–S–Sb-bearing solutions could migrate through cracks and the interconnected network of pores in the chromitite. However, the mobility of these PGE- and Ni–As–S–Sb-bearing solutions must be very limited, as indicated by the presence of minute grains of PGE-rich and Ni–As–Sb compounds in the proximities of larger altered PGMs (e.g., Fig. 10o–p). This is explained by the strong tendency of As and Sb to immobilise PGEs and noble metals such as Au, as in low-temperature hydrothermal fluids these metalloids will readily combine with the precious metals to form stable compounds (Wood, 2002; Reich et al., 2005; Deditius et al., 2014).

On the other hand, the occurrence of grains of native gold along cracks or interstices porous chromite (Fig. 10u–w) support a secondary origin related with metamorphic fluids. Although some grains of native gold have been described as inclusions in primary chromites (e.g., Graham et al., 1996; Gervilla et al., 2002), secondary hydrothermal enrichment in gold is a distinctive feature of metamorphosed chromitites (Thalhammer et al., 1990; Tarkian et al., 1991; Yang and Seccombe, 1993; Graham et al., 1996; Malitch et al., 2001). The possible sources for gold in the La Cabaña chromitites could be: (1) primary gold present in solid solution or as nano to submicron particles within magmatic chromite and/or refractory sulphide inclusions (Reich et al., 2006; Hough et al., 2012), and (2) metamorphic fluids sourced from the country metasedimentary rocks which may also contain mesothermal gold mineralizations. Remobilization during metamorphism might have had an unforeseen impact on Au and associated metals at La Cabaña. Although circumstantial, the occurrence of Pd, Hg, and Bi-bearing phases filling factures and pores in secondary chromite is compelling, and further studies are needed to constrain the source of metals and remobilization/reconcentration processes.

5.6. Linking (PGE–Au) ± Ni–As–Sb mineralization in the chromitites to their metamorphic evolution within the Paleozoic accretionary complex

The geology and tectonic evolution of the Chilean Coastal Cordillera indicate that during the Late Paleozoic the chromitite-bearing ultramafic bodies and their metasedimentary host rocks were part of an accretionary complex developed at the southwestern margin of Gondwana (Hervé et al., 1976; Hervé, 1977; Godoy, 1979; Hyppolito et al., 2014a,b). Within this context, the serpentinites were mixed tectonically within the metasedimentary rocks during polyphase, more or less continuous development of subduction channel (Höfer et al., 2001). A conceptual model sketching this possible scenario is shown in Fig. 18.

During subduction, drifting associated with cornerflow may produce downwards movement of the sub-arc peridotitic rocks, while large volumes of fluid can be released by dehydration of the subducting oceanic crust. The main dewatering takes place at temperatures between 300 and 600 °C and pressures lower than 15 kbar (Rüpke et al., 2004). The upward percolation of these fluids may induce hydration of the overlying peridotite wedge, giving rise to *mantle wedge* serpentinites with characteristic trace-element profiles enriched in FME (including B, Cs, As, Sb, Pb, Li; Fig. 4; Deschamps et al., 2012, 2013). The olivine–lizardite dunites from the Centinela Bajo Norte body show similar patterns to this type of mantle wedge serpentinites (Fig. 4), suggesting that they could represent portions of a mantle wedge that once overly the subducting slab (point 1 in Fig. 18). The local replacement of olivine by mesh lizardite in our samples suggests that these early phases of hydration took place due to infiltration of Si-poor fluids at low fluid/rock ratios (i.e., quasi-isochemical) and temperatures (<300 °C) within the upper 3–6 km of the slab (i.e., <3.5 kbar; Bach et al., 2004, 2006; Evans et al., 2013).

Continued movement downward of the already hydrated sub-arc lithosphere promotes burial of the partially serpentinized peridotites while they are progressively heated (i.e., prograde metamorphism; point 2 in Fig. 18). The formation of schistose antigorite-rich serpentinites suggests a fault-controlled fluid flow and deformation. This was most likely related to the infiltration of progressively hotter fluids in shear zones throughout the subduction channel (Blanco-Quintero et al., 2011 and references therein), because formation of antigorite in the developing shear zones is favoured due to focusing of deformation (Ribeiro da Costa et al., 2008; Auzende et al., 2015). At this stage, more silica-rich fluids would enhance the direct replacement of relict olivine (±lizardite) to antigorite and pyroxene to talc + tremolite (Trommsdorff and Evans, 1972, 1974; Bach et al., 2004, 2006; Evans et al., 2013; Nagaya et al., 2014) while promoting the reaction of the chromite with the olivine matrix to produce the secondary assemblage of porous chromite + chlorite (Fig. 15). According to our thermodynamical modelling, peak conditions should have taken place at ~510–560 °C.

Moreover, the temperatures range of 520–550 °C estimated by Höfer et al. (2001) for the formation of Si-metasomatic blackwalls along the boundaries of the chromitite-bearing ultramafic bodies suggest that SiO_2-rich fluids could have emanated from the country rocks at this stage. The schistose antigorite (±talc) serpentinite filling the shear zones containing the chromite ores are abnormally enriched in As and Sb relative to the olivine–lizardite dunites, and in turn to other serpentinites produced by slab-derived fluid metasomatism of the mantle wedge in suprasubduction zones (grey field in Fig. 4a). Disregarding the possible effects of the serpentinite structure in accommodating the different metals, this particular signature led us to suggest a different source for the fluids that have produced the alteration. According to the data in the As vs. Sb plot of Fig. 17 a sedimentary source is the

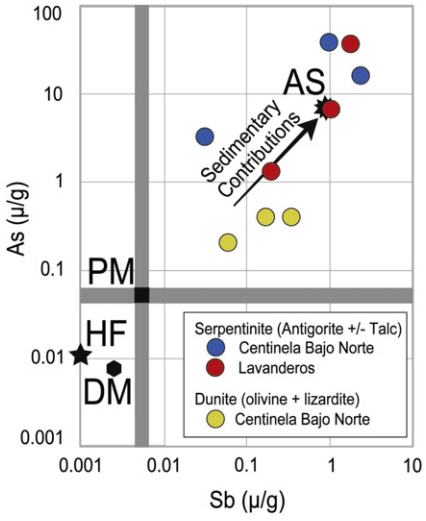

Fig. 17. As vs. Sb concentrations (expressed as µg g^{-1}) for the ultramafic rocks of the La Cabaña area. This figure is a modification from Deschamps et al. (2011) and the keys are: DM: depleted mantle (Salters and Stracke, 2004), HF: Logatchev Hydrothermal fluid (Schmidt et al., 2007), AS: average composition of sediments from the Argo abyssal plain at site 765 (Plank and Ludden, 1992). Grey field are mantle wedge serpentinites with dunite protolith (Deschamps et al., 2013).

main candidate for the infiltrating fluids. This is consistent with preliminary stable chlorine isotope studies that indicate that fluids responsible for the serpentinization of the Lavanderos ultramafic body are sedimentary pore-fluids, possibly released and heated during metamorphism (Barra et al., 2012; Salazar, 2015). These observations support the notion that fluids emanated during metamorphism of the enclosing sediments could be injected through the shear zones adding Si and metalloids such as As, Sb, Pb, Zn and Hg. The presence of Sb-rich orcelite intergrown with antigorite (Fig. 5a–d) and porous chromite (Fig. 5e–f) in schistose antigoritite also supports a link with the formation of prograde serpentinite. Furthermore, local formation of birbirite associated with the chromitites of Centinela Bajo Norte indicates circulation of highly Si-enriched fluids.

Another possibility is that the silica-rich environment required to produce the antigorite and tremolite + talc lithologies was produced as a consequence of the percolation of fluids through pyroxene-bearing dunite or harzburgite protoliths. In this alternative scenario, the hydrothermal fluids that infiltrated the serpentinites may have also leached As, Sb and others metals, as hundreds of ppm of As, Sb, Pb and Zn can be contained in the structure of the serpentine (Hattori and Guillot, 2007; Hattori et al., 2005; Kodolanyi et al., 2011; Deschamps et al., 2013) or in discrete sulphides hosted in the serpentinite (Bukhard, 1989; Hattori et al., 2002; Blusztajn et al., 2014). These fluids could leach the metals from the serpentinite and later deposit the metals in the shear zones representing structurally favourable domains.

The temperatures derived above for the formation of the porous chromite and the blackwalls (point 2 in Fig. 18) are slightly higher than the metamorphic peak conditions of ~420 °C at 8–9 kbar estimated for the metasedimentary host rocks in the Western Series (Willner et al., 2001, 2005; Willner, 2005; Glodny et al., 2008). This suggests that in the early stages of exhumation within the accretionary prism non-isofacial rocks coexisted, i.e., hotter ultramafic bodies were tectonically mixed with cooler metasediments. The existence of a thermal gradient between the peridotites and their country rocks would facilitate the element exchange necessary to produce the observed blackwalls at the contact between ultramafic bodies and the host metapelitic schist. According to Höfer et al. (2001) and field-work observations resulting from this study, the main schistosity planes of the latest stages of deformation in the serpentinites and the host micachists are identical, suggesting a common history of deformation after tectonic mixing of these rocks. In contrast, the large window of temperatures from ~430 °C down to ~200 °C estimated using chlorite and sulphide geothermometry included in porous chromite clearly overlap the greeenchist retrograde overprint that affected the rocks of the Western Series. According to Willner (2005) the metasedimentary rocks of the southern section (38–43°S) of the Western Series recorded a retrograde overprint at 300–400 °C with pressure release of ~3–4 kbar. Fluid inclusions studies by Collao and Alfaro (2000) in quartz from volcanic massive sulphide deposits (VMS) and enclosing metasedimentary rocks from the Nahuelbuta and Queule Mountains (50 km west from La Cabaña area) have reported similar metamorphic pathway with a peak at 390–410 °C at 9.0 kbar and retrograde overprint at 290–270 °C at ~3.5 kbar. All these observations together clearly indicate that the ultramafic rocks and the enclosing metasedimentary rocks had a common metamorphic history of exhumation, confirming the observations by Höfer et al. (2001).

Summarizing the arguments presented above, we propose a conceptual model where ultramafic bodies were tectonically juxtaposed with the metasediments, and were exhumed together. Therefore, exhumation of the entire ultramafic body took place in two stages. The first stage mostly likely occurring along the subduction channel (point 2 to 3 in Fig. 18), and could take place almost coevally with the high-pressure metamorphism of the metasedimentary rocks (see review of Hyppolito et al., 2014a,b). The presence of (PGE-bearing) Ni/rich sulpharsenides and antimonides in porous chromite suggests that this is when Ni-, As, and Sb-bearing fluids infiltrated the chromitites, reacting with the pre-existing PGM mineralogy while precipitating the precursor Ni-rich *mss*. The second stage corresponded to a slower exhumation (point 3 to 4 in Fig. 18) associated with underplating processes and erosion when the prism was already well established (Glodny et al., 2005), and during which the ultramafic and host rocks cooled. Antigorite may have been stable along the exhumation trajectory until it reached the 300 °C isotherm at 3.5 kbar, which marks the lower stability of this mineral (Agrinier and Cannat, 1997; Agrinier et al., 1995; Früh-Green et al., 1996; Evans et al., 2013) and the minimum PT conditions of the greenchist facies overprint (point 3 in Fig. 18). Continued cooling associated with exhumation (from point 2 to 3 in Fig. 18) resulted in the subsolidus re-equilibration of the secondary (PGE–Au) ± Ni–As–Sb, as indicated by the formation of different Ni-rich sulphide ± Ni-rich sulpharsenide polymorphs at ~300 °C (point 3 in Fig. 18). A post-antigorite serpentinization veining event, related with the

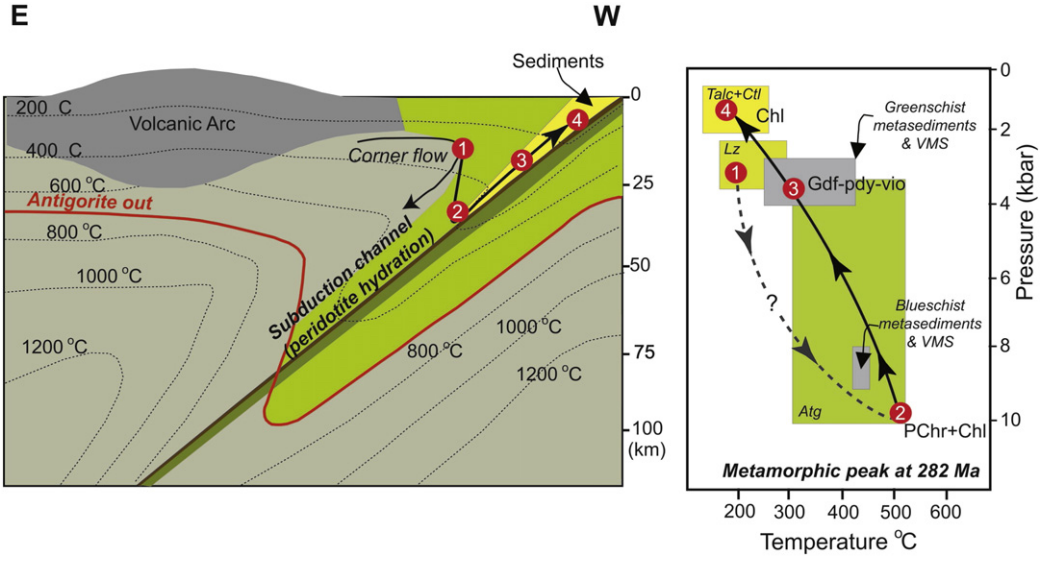

Fig. 18. Schematic cross-section showing the tectonic configuration of the Paleozoic subduction zone in south-central Chile and the proposed model for the origin of the studied rocks. The thermal structure of the subduction zone and the stability of serpentinite is an adaptation from Blanco-Quintero et al. (2011). Abbreviations: Atg: antigorite, Chl: chlorite, Ctl: chrysotile, Gdf: gersdorffite, Lz: lizardite, Ni-mss: Ni-rich monosulphide solid solution, P-Chr: porous chromite.

circulation of late hydrothermal fluids (<250 °C; Evans, 2010) during brittle deformation (Willner, 2005), may have produced the veins of chrysotile and a second generation of talc (Fig. 3f) while fracturating of chromite grains (Fig. 6a–b) postdated all the previous minerals during emplacement of the ultramafic massifs in the shallow crust (point 4 in Fig. 18).

6. Concluding remarks

(1) The chromitites observed in situ in the La Cabaña ultramafic bodies are associated with shear zones filled with antigorite (± talc) serpentinites that isolate blocks of peridotite partly altered to lizardite. Fluid-assisted deformation during the development of the shear zones has resulted in the alteration of the magmatic chromite to two microstructural types of chromite. Type A chromite preserves magmatic cores and mildly deformed porous rims characterized by low degrees of misorientation (≤2°), whereas Type B chromite is porous and shows coupling between greater deformation (misorientation degrees between 2 and 8°) and chemical modification. An estimate of the temperatures of alteration of chromite using thermodynamic modelling suggests the reaction of chromite with the olivine matrix to produce the pair porous chromite + chlorite at 510–560 °C.

(2) The metamorphic porous chromite contains abundant inclusions of platinum-group minerals and gold. Only a few crystals of osmium and one laurite were found in the unaltered cores of Type A chromite, suggesting that they were unaffected by metamorphic fluids. Most PGMs observed in the porous chromites were either recrystallised or newly formed during the infiltration of metamorphic hydrothermal fluids. Gold grains are exclusively found in porous chromite or filling sealed fractures in chromite grains, clearly suggesting a secondary origin related with metamorphism. Geothermometry of chlorite associated with these secondary PGMs yielded temperatures varying from ~430 to 188 °C, in good agreement with temperatures estimated from the equilibria of different mineral inclusions of the Ni–Fe–As–S system, associated with PGMs and/or chlorite in the metamorphic porous chromite.

(3) The range of temperatures estimated for the formation of porous chromite is higher than the peak metamorphic temperature of the metasediments hosting the chromitite-bearing ultramafic bodies (i.e., ~420 °C, 9.3 kbar). This is interpreted as a result of the intrusion of the hotter exhuming ultramafic body transported in the subduction channel into cooler sediments of the accretionary prism. In contrast the temperature window from ~400 down to ~200 °C is consistent with the retrograde greenschist-facies metamorphism that affected both the chromitite-bearing ultramafic bodies and their enclosing host rocks.

(4) The origin of the (PGE–Au) ± Ni–As–Sb mineralization is directly linked to the metamorphic evolution of the chromitites within a developing accretionary prism. Structural relationships of the shear zones together with the geochemistry and mineralogy of the serpentinite suggest that fluids released from the metasediments during metamorphism were channeled through these favourable discontinuities, producing the observed alteration pattern in chromite and their associated secondary noble and base-metal mineralization.

Supplementary data to this article can be found online at http://dx.doi.org/10.1016/j.oregeorev.2016.02.017.

Acknowledgements

We acknowledge Idael F. Blanco-Quintero, Ibrahim Uysal and an anonymous referee for their critical review that greatly improved the quality of this manuscript. Editor-in-Chief Franco Pirajno is also thanked by helping the final editing of this research paper. This research has been financially supported by a Fondecyt Initiation Grant #11140005 to J.M. González-Jiménez entitled "*Decoding precious metals (platinum-group elements and gold) in upper mantle rocks of the Chilean Cordillera*" and Fondecyt Grant #1110345, entitled "*Origin and evolution of the Coastal Cordillera ophiolite complex, Central Chile*" to F. Barra. Additional support was provided by the MSI "Millennium Nucleus for Metal Tracing along Subduction" (NC130065) headed by M. Reich. This is a contribution of the ARC National Key Centre for Geochemical Evolution and Metallogeny of Continents (www.es.mq.edu.au/GEMOC) and the ARC Centre of Excellence for Core to Crust Fluid Systems.

References

Agrinier, P., Cannat, M., 1997. Oxygen-isotope constraints in serpentinization processes in ultramafic rocks from the Mid-Atlantic Ridge (23°N). Proc. Ocean Drill. Program Sci. Results 153, 381–388.

Agrinier, P., Hékinian, R., Bideau, D., Javoy, M., 1995. Stable isotope compositions ($^{18}O/^{16}O$, D/H, and $^{13}C/^{12}C$) of oceanic crust and upper mantle rocks exposed in the Hess Deep near the Galapagos Triple Junction. Earth Planet. Sci. Lett. 136, 183–196.

Aguirre, L., Hervé, F., Godoy, E., 1972. Distribution of metamorphic facies in Chile, an outline. Kristalinikum 9, 7–19.

Aiglsperger, T., Proenza, J.A., Zaccarini, F., Lewis, J.F., Garuti, G., Labrador, M., Longo, F., 2015. Platinum group minerals (PGM) in the Falcondo Ni-laterite deposit, Loma Caribe peridotite (Dominican Republic). Mineral. Deposita 50, 105–123.

Alfaro, G., 1980. Antecedentes preliminares sobre la composición y génesis de las cromitas de La Cabaña (Cautín). Rev. Geol. Chile 11, 29–41.

Alfaro, G., 1981. Exploración del Cuerpo Ultramáfico de La Cabaña (Cautín). Inst. Invest. Geol. (Internal Rep.) (11 pp.).

Álvarez, O., Rivera, A., 1970. Informe preliminary de la primera etapa de estudios de anomalías magnéticas y radiométricas detectadas en la region de la Cordillera de la Costa, entre rio Imperial y el extreme sur de la Isla de Chiloé. Inst. Invest. Geol. (unpublished), 25 pp.

Andrews, D.R.A., Brenan, J.M., 2002. Phase-equilibrium constraints on the magmatic origin of laurite + Ru–Os–Ir alloy. Can. Mineral. 40, 1705–1716.

Augé, T., Joubert, M., Bailly, L., 2012. Typology of mafic–ultramafic complexes in Hoggar, Algeria: implications for PGE, chromite and base-metal sulphide mineralisation. J. Afr. Earth Sci. 63, 32–47.

Auzende, A.-L., Escartin, J., Walte, N., Guillot, S., Hirth, G., Frost, J., 2015. Deformation mechanism of antigorite serpentinite at subduction zone conditions determined from experimentally and naturally deformed rocks. Earth Planet. Sci. Lett. 411, 229–240.

Bach, W., Garrido, C.J., Paulick, H., Harvey, J., Rosner, M., 2004. Seawater peridotite interactions: first insights from ODP Leg 209, MAR 15°N. Geochem. Geophys. Geosyst. 5, Q09F06. http://dx.doi.org/10.1029/2004GC000744.

Bach, W., Paulick, H., Garrido, C.J., Ildefonse, B., Meurer, W.P., Humphris, S.E., 2006. Unraveling the sequence of serpentinization reactions: petrography, mineral chemistry, and petrophysics of serpentinites from MAR 15°N (ODP Leg 209, Site 1274). Geophys. Res. Lett. 33, L13306.

Ballhaus, C., Ulmer, P., 1995. Platinum-group elements in the Merensky reef: II. Experimental solubilities of platinum and palladium in $Fe_{1-x}S$ from 950 to 450 °C under controlled fS_2 and fH_2. Geochim. Cosmochim. Acta 59, 4881–4888.

Barnes, S.J., Fiorentini, M.L., 2008. Iridium, ruthenium and rhodium in komatiites: evidence for iridium alloy saturation. Chem. Geol. 257, 44–58.

Barra, F., Rabbia, O., Alfaro, G., Miller, H., Höfer, C., Kraus, S., 1998. Las serpentinitas y cromititas de La Cabaña, provincia de Cautín. Chile. Rev. Geol, Chile, IX Región.

Barra, F., Barnes, J., Reich, M., 2012. The serpentinites from the Coastal Cordillera of south-central Chile — a preliminary report. AGU Fall Meeting Abstracts Vol. 1, p. 2809.

Barra, F., Gervilla, F., Hernández, E., Reich, M., Padrón-Navarta, J.A., 2014. Alteration patterns of chromian spinels from La Cabaña peridotite, south-central Chile. Mineral. Petrol. 108 (6), 819–836. http://dx.doi.org/10.1007/s00710-014-0335-5.

Blanco-Quintero, I.F., Proenza, J.A., Garcia-Casco, A., Tauler, E., Galí, S., 2011. Serpentinites and serpentinites within a fossil subduction channel: La Corea mélange, eastern Cuba. Geol. Acta http://dx.doi.org/10.1344/10.1344/105.000001662.

Blusztajn, J., Shimizu, N., Warren, J.M., Dick, H.J.B., 2014. In-situ Pb isotopic analysis of sulphides in abyssal peridotites: new insights into heterogeneity and evolution of the oceanic upper mantle. Geology 42, 159–162.

Bockrath, C., Ballhaus, C., Holzheid, A., 2004. Stabilities of laurite RuS_2 and monosulphide liquid solution at magmatic temperature. Chem. Geol. 208, 265–271.

Brenan, J.M., Andrews, D., 2001. High-temperature stability of laurite and Ru–Os–Ir alloy and their role in PGE fractionation in mafic magmas. Can. Mineral. 39, 341–360.

Bukhard, D.J.M., 1989. Co–Ni–As sulphides in serpentinites of different metamorphic grade in the eastern central Alps (Switzerland and Italy). Mineral. Petrol. 41, 65–71.

Cassard, D., Nicolas, A., Rabinowicz, M., Moutte, M., Leblanc, M., Prinzhofer, A., 1981. Structural classification of chromite pods in southern New Caledonia. Econ. Geol. 76, 805–831.

Cathelineau, M., 1988. Cation site occupancy in chlorites and illites as a function of temperature. Clay Miner. 23, 471–485.
Cathelineau, M., Nieva, D., 1985. A chlorite solid solution geothermometer. The Los Azufres (Mexico) geothermal system. Contrib. Mineral. Petrol. 91, 235–244.
Christiansen, F., 1986. Structures of Ophiolitic Chromite Deposits (Ph.D. Thesis) Aarhus University, Denmark (84 pp.).
Collao, R., Alfaro, G., 2000. Paleozoic massive sulphide orebodies of the Nahuelbuta and Queule mountains, South-Central Chile: results of geobarometry and sulphur isotope studies. In: Sherlock, R., Logan, M.A.V. (Eds.), VMS Deposits of Latin America, Geol. Association of Canada, Spec. Pub. Vol. 2, pp. 629–641
Connolly, J.A.D., 2009. The geodynamic equation of state: what and how. Geochem. Geophys. Geosyst. 10, Q10014. http://dx.doi.org/10.1029/2009GC002540.
Craig, J.R., 1971. Violarite stability relations. Am. Mineral. 56, 1303–1311.
Craig, J.R., 1973. Pyrite–pentlandite assemblages and other low temperature relations in the Fe–Ni–S system. Am. J. Sci. 273A, 496–510.
Deditius, A., Reich, M., Kesler, S.E., Utsunomiya, S., Chryssoulis, S., Walshe, J.L., Hough, R., Ewing, R.C., 2014. The coupled geochemistry of Au and As in pyrite from hydrothermal ore deposits. Geochim. Cosmochim. Acta 140, 644–670.
Deschamps, F., Guillot, S., Godard, M., Andreani, M., Hattori, K., 2011. Serpentinites act as sponges for fluid-mobile elements in abyssal and subduction zone environments. Terra Nova 23 (3), 171–178. http://dx.doi.org/10.1111/j.1365-3121.2011.00995.x.
Deschamps, F., Godard, M., Guillot, S., Chauvel, C., Andreani, M., Hattori, K., Wunder, B., France, L., 2012. Behavior of fluid-mobile elements in serpentines from abyssal to subduction environments: examples from Cuba and Dominican Republic. Chem. Geol. 312–313, 93–117.
Deschamps, F., Godard, M., Guillot, S., Hattori, K., 2013. Geochemistry of subduction zone serpentinites: a review. Lithos 178, 96–127. http://dx.doi.org/10.1016/j.lithos.2013.05.019.
Drury, M.R., Urai, J.L., 1990. Deformation-related recrystallization processes. Tectonophysics 172, 35–253.
El Ghorfi, M.L., Melcher, F., Oberthür, T., Boukhari, A.E., Maacha, L., Maddi, A., Mhaili, M., 2008. Platinum group minerals in podiform chromitites of the Bou Azzer ophiolite, Anti Atlas, Central Morocco. Mineral. Petrol. 92, 59–80.
Engi, M., 1983. Equilibria involving Al–Cr spinel: Mg–Fe exchange with olivine. Experiments, thermodynamic analysis, and consequences of geothermometry. Am. J. Sci. 283A, 20–71.
Evans, B.W., 2010. Lizardite versus antigorite serpentinite: magnetite, hydrogen, and life (?). Geology 38, 879–882.
Evans, B.W., Hattori, K., Baronnet, A., 2013. Serpentinite: what, why, where? Elements 9, 99–106.
Finnigan, C.S., Brenan, J.M., Mungall, J.E., McDonough, W.F., 2008. Experiments and models bearing on the role of chromite as a collector of platinum group minerals by local reduction. J. Petrol. 49, 1647–1665.
Fleet, M.E., 2006. Phase equilibria at high temperaturas. Rev. Mineral. Geochem. 61, 365–419.
Fonseca, R.O.C., Laurenz, V., Mallmann, G., Luguet, A., Hoehne, N., Jochum, K.P., 2012. New constrains on the genesis and long-term stability of Os-rich alloys in the Earth's mantle. Geochim. Cosmochim. Acta 87, 227–242.
Früh-Green, G.L., Plas, A., Lecuyer, C., 1996. Petrologic and stable isotopic constraints on hydrothermal alteration and serpentinization of the EPR shallow mantle at Hess Deep, Site 895. Proc. Ocean Drill. Program Sci. Results 147, 109–163.
Frutos, J., Alfaro, G., 1987. Metallogenetic and tectonic chracteristics of the Paleozoic ophiolitic belt of the southern Chile coast cordillera. Geol. Rundsch. 76, 343–356.
Galdames, C., Rabbia, O.M., Alfaro, G., Hernández, L., 2011. Platinum-group elements in ultramafic rocks from La Cabaña area, Coastal Cordillera of South-Central Chile. Eleventh International Platinum Symposium: Ontario Geological Survey, Miscellaneous Release—Data, p. 269.
Gao, S., Liu, X., Yuan, H., Hattendorf, B., Günther, D., Chen, L., Hu, S., 2002. Determination of forty two major and trace elements in USGS and NIST SRM glasses by Laser Ablation-Inductively Coupled Plasma-Mass Spectrometry. Geostand. Newslett. 26 (2), 181–196.
Garuti, G., Zaccarini, F., 1997. In situ alteration of platinum-group minerals at low temperature: evidence from serpentinized and weathered chromitite of the Vourinos complex, Greece. Can. Mineral. 35, 611–626.
Gervilla, F., Gutiérrez-Narbona, R., Fenoll Hach-Ali, P., 2002. The origin of different types of magmatic mineralizations from small-volume melts in the lherzolite massifs of the serranna de Ronda. J. Span. Min. Soc. 25, 79–96.
Gervilla, F., Proenza, J.A., Frei, R., González-Jiménez, J.M., Garrido, C.J., Melgarejo, J.C., Meibom, A., Díaz-Martínez, R., Lavaut, W., 2005. Distribution of platinum-group elements and Os isotopes in chromite ores from Mayarí–Baracoa Ophiolite Belt (eastern Cuba). Contrib. Mineral. Petrol. 150, 589–607.
Gervilla, F., Padrón-Navarta, J.A., Kerestedjian, T., Sergeeva, I., González-Jiménez, J.M., Fanlo, I., 2012. Formation of ferrian chromite in podiform chromitites from the Golyamo Kamenyane serpentinite, Eastern Rhodopes, SE Bulgaria: a two-stage process. Contrib. Mineral. Petrol. 164, 643–657.
Ghosh, B., Konar, R., 2012. Textural developments in chromite deforming under eclogite facies conditions from the Neoarchaean Sittampundi anorthosite complex, southern India. Geol. J. 47, 253–262.
Ghosh, B., Morishita, T., Bhatta, K., 2013. Significance of chromian spinels from the mantle sequence of the Andaman Ophiolite, India: paleogeodynamic implications. Lithos 164–167, 86–96.
Ghosh, B., Ray, J., Morishita, T., 2014. Grain-scale plastic deformation of chromite from podiform chromitite of the Naga–Manipur ophiolite belt, India: implication for mantle dynamics. Ore Geol. Rev. 56, 199–208.
Glennie, K.W., Boeuf, M.G.A., Hughes Clarke, M.W., Moody-stuart, M., Pilaar, W.F.H., Reinhardt, B.M., 1974. Geology of the Oman Mountains. Koninkl. Nederlands Geol. Mijnbouwkundig Genoot. Verh. 31 (2), 1–423.
Glodny, J., Lohrmann, J., Echtler, H., Gräfe, K., Seifert, W., Collao, S., Figueroa, O., 2005. Internal dynamics of a paleoaccretionary wedge: insights from combined isotope tectonochronology and sandbox modelling of the South-Central Chilean forearc. Earth Planet. Sci. Lett. 231, 23–39.
Glodny, J., Echtler, H., Collao, S., Ardiles, M., Burón, P., Figueroa, O., 2008. Differential Late Paleozoic active margin evolution in South-Central Chile (37°S–40°S) — the Lanalhue Fault Zone. J. S. Am. Earth Sci. 26, 397–411.
Godoy, E., 1979. Metabasitas del basamento metamórfico. Congreso Geológico Chileno Vol. 2(3), pp. E133–E144.
González-Jiménez, J.M., Gervilla, F., Proenza, J.A., Augé, T., Kerestedjian, T., 2009. Distribution of platinum-group minerals in ophiolitic chromitites. Appl. Earth Sci. 118, 101–110.
González-Jiménez, J.M., Gervilla, F., Kerestedjian, T., Proenza, J.A., 2010. Alteration of platinum-group and base-metal mineral assemblages in ophiolite chromitites from the Dobromirtsi Massif, Rhodope Mountains (Bulgaria). Res. Geol. 60, 315–334. http://dx.doi.org/10.1111/j.1751-3928.2010.00138.x.
González-Jiménez, J.M., Marchesi, C., Griffin, W.L., Gutiérrez-Narbona, R., Lorand, Jean-P, O'Reilly, S.Y., Garrido, C.J., Gervilla, F., Pearson, N.J., Hidas, K., 2013. Transfer of Os isotopic signatures from peridotite to chromitite in the subcontinental mantle: insights from in situ analysis of platinum-group and base-metal minerals (Ojén peridotite massif, southern Spain). Lithos 164–167, 74–85. http://dx.doi.org/10.1016/j.lithos.2012.07.009.
González-Jiménez, J.M., Barra, F., Walker, R.J., Reich, M., Gervilla, F., 2014a. Geodynamic implications of ophiolitic chromitites in the La Cabaña ultramafic bodies, Central Chile. Int. Geol. Rev. 56, 1466–1483.
González-Jiménez, J.M., Griffin, W.L., Proenza, J.A., Gervilla, F., O'Reilly, S.Y., Akbulut, M., Pearson, N.J., Arai, S., 2014b. Chromitites in ophiolites: how, where, when, why? Part II. The crystallization of chromitites. Lithos 189, 140–158. http://dx.doi.org/10.1016/j.lithos.2013.09.008.
Graham, I.T., Franklin, B.J., Marshall, B., 1996. Chemistry and mineralogy of podiform chromitite deposits, southern NSW, Australia: a guide to their origin and evolution. Mineral. Petrol. 57, 129–150.
Grieco, G., Diella, V., Chaplygina, N.L., Savalieva, G.N., 2006. Platinum group elements zoning and mineralogy of chromitites from the cumulate sequence of the Nurali massif (Southern Urals, Russia). Ore Geol. Rev. 30, 257–276.
Griffin, W., Powell, W., Pearson, N., O'Reilly, S., 2008. GLITTER: data reduction software for laser ablation ICP-MS. In: Sylvester, P. (Ed.), Laser Ablation-ICP-MS in the Earth Sciences. Mineral. Assoc. Canada Short Course Series Vol. 40, pp. 204–207.
Gutierrez-Narbona, R., Lorand, J.-P., Gervilla, F., Gros, M., 2003. New data on base-metal mineralogy and platinum-group minerals in the Ojen chromitites (Serranía de Ronda, Betic Cordillera, southern Spain). Neues Jb. Mineral. Abh. 179, 143–173.
Hattori, K., Guillot, S., 2007. Geochemical character of serpentinites associated with high-to ultrahigh-pressure rocks in the Alps, Cuba, and the Himalayas: recycling of elements in subduction zones. Geochem. Geophys. Geosyst. 8 (9), Q09010. http://dx.doi.org/10.1029/2007GC00159.
Hattori, K.H., Arai, S., Clarke, D.B., 2002. Selenium, tellurium, arsenic and antimony contents of primary mantle sulfides. Can. Mineral. 40, 637–650.
Hattori, K.H., Takahashi, Y., Guillot, S., Johanson, B., 2005. Occurrence of arsenic (V) in forearc mantle serpentinites based on X-ray absorption spectroscopy study. Geochim. Cosmochim. Acta 69, 5585–5596.
Hervé, F., 1974. Petrology of the Crystalline Basement Nahuelbuta Mountains, South-Central Chile (PhD Thesis) University of Hokkaido.
Hervé, F., 1977. Petrology of the crystalline basement of the Nahuelbuta Mountains, southcentral Chile. In: Ishikawa, T., Aguirre, L. (Eds.), Comparative Studies on the Geology of the Circum Pacific Orogenic Belt in Japan and Chile. Tokyo, Japan Society for the Promotion of Science, pp. 1–51.
Hervé, F., Godoy, E., Del Campo, M., Ojeda, J., 1976. Las metabasitas del basamento metamórfico de Chile Central y Austral. I Congreso Geológico Chileno Vol. 1(1), pp. F175–F187.
Hervé, F., Munizaga, F., Parada, M.A., Brook, M., Pankhurst, R., Snelling, N., Drake, R., 1988. Granitoids of the Coast Range of central Chile: geochronology and geologic setting. J. S. Am. Earth Sci. 1, 185–194. http://dx.doi.org/10.1016/0895-9811(88)90036-3.
Hervé, F., Calderón, M., Fanning, C.M., Pankhurst, R.J., Godoy, E., 2013. Provenance variations in the Late Paleozoic accretionary complex of central Chile as indicated by detrital zircons. Gondwana Res. 23, 1122–1135. http://dx.doi.org/10.1016/j.gr.2012.06.016.
Hey, M.H., 1954. A new review of the chlorites. Mineral. Mag. 30, 277–292.
Höfer, C., Kraus, S., Miller, H., Alfaro, G., Barra, F., 2001. Chromite-bearing serpentinite bodies within an arc–backarc metamorphic complex near La Cabaña, south Chilean Coastal Cordillera. J. S. Am. Earth Sci. 14 (1), 113–126. http://dx.doi.org/10.1016/S0895-9811(01)00011-6.
Holland, T., Powell, R., 1998. An internally consistent thermodynamic data set for phases of petrological interest. J. Metamorph. Geol. 16 (3), 309–343.
Hough, R., Reich, M., Noble, R., 2012. Noble Metal Nanoparticles in Ore Systems. In: Barnard, Amanda S., Guo, Haibo (Eds.), In Nature's Nanostructures. Pan Stanford Publishing Pte. Ltd. ISBN 978-981-4316-82-8, pp. 141–167.
Hull, D., Rimmer, D.E., 1959. The growth of grain-boundary voids under stress. Philos. Mag. 4 (42), 673–687.
Hyppolito, T., García-Casco, A., Juliani, C., Meira, V.T., Hall, C., 2014a. Late Paleozoic onset of subduction and exhumation at the western margin of Gondwana (Chilenia Terrane): counterclockwise P–T paths and timing of metamorphism of deep-seated garnet–micha schist and amphibolite of Punta Sirena, Coastal Accretionary Complex, Central Chile (34° S). Lithos 206–207, 409–434.
Hyppolito, T., Juliani, C., García-Casco, A., Meira, T.V., Bustamante, A., Hervé, F., 2014b. The nature of the Paleozoic oceanic basin at the southwestern margin of Gondwana and

implications for the origin of the Chilenia terrane (Pichilemu region, central Chile). Int. Geol. Rev. 56, 1097–1121.
Klein, E.L., Koppe, J.C., 2000. Chlorite geothermometry and physicochemical conditions of gold mineralization in the Paleoproterozoic Caixas deposit, São Luis Craton, northern Brazil. Geochim. Bras. 12, 219–232.
Klemm, D.D., 1965. Synthesen und Analysen in den Dreiecksdiagrammen FeAsS–CoAsS–NiAsS und FeS_2–CoS_2–NiS_2. Neues Jahrb. Mineral. Abh. 103, 205–255.
Klemme, S., Ivanic, T.J., Connolly, J.A.D., Harte, B., 2009. Thermodynamic modelling of Cr-bearing garnets with implications for diamond inclusions and peridotite xenoliths. Lithos 112, 986–991.
Kodolanyi, J., Pettke, T., Spandler, C., Kamber, B.S., Gméling, K., 2011. Geochemistry of ocean floor and fore-arc serpentinites: constraints on the ultramafic input to subduction zones. J. Petrol. http://dx.doi.org/10.1093/petrology/egr058.
Kranidiotis, P., MacLean, W.H., 1987. Systematics of chlorite alteration at the Phelps Dodge massive sulfide deposit, Mattagami, Quebec. Econ. Geol. 82, 1898–1911.
Kullerud, G., Yund, R.A., 1962. The Ni–S system and related minerals. J. Petrol. 3, 126–175.
Leblanc, M., 1991. Platinum-group elements and gold in ophiolitic complexes: distribution and fractionation from mantle to oceanic floor. In: Petters, T.J. (Ed.)Ophiolite Genesis and Evolution of the Oceanic Lithosphere Vol. 5. Kluwer Academic Publ., Dordrecht, The Netherlands, pp. 231–260.
Lockwood Survey Co., 1969. Airborne magnetometer ± scintillation counter survey. Report for Instituto de Investigaciones Geológicas, Santiago de Chile (99 pp., 83 maps).
Locmelis, M., Pearson, N.J., Barnes, S.J., Florentini, M.L., 2011. Ruthenium in komatiic chromite. Geochim. Cosmochim. Acta 75, 3645–3661.
Lorand, J.P., Alard, O., Luguet, A., 2010. Platinum-group element micronuggets and refertilization process in Lherz orogenic peridotite (northeastern Pyrenees, France). Earth Planet. Sci. Lett. 289, 298–310.
Makovicky, M., Makovicky, E., Rose-hansen, J., 1986. Experimental studies on the solubility and distribution of platinum-group elements in base-metal sulphides in platinum deposits. In: Gallagher, M.J., Ixer, R.A., Neary, C.R., Prichard, H.M. (Eds.), Metallogeny of Basic and Ultrabasic Rocks. London, U.K., The Institution of Mining and Metallurgy, pp. 415–425.
Makovicky, M., Makovicky, E., Rose-Hansen, J., 1988. Experimental evidence of the formation and mineralogy of platinum and palladium ore deposits. In: Boissonnas, J., Omenetto, P. (Eds.), Mineral Deposits Within the European Community. Springer-Verlag, Berlin, Germany, pp. 303–317.
Malitch, K.N., Melcher, F., Mühlhans, H., 2001. Palladium and gold mineralization in podiform chromitite at Kraubath, Austria. Mineral. Petrol. 73, 247–277.
Melcher, F., Grum, W., Simon, G., Thalhammer, T.V., Stumpfl, E.F., 1997. Petrogenesis of the ophiolitic giant chromite deposits of Kempirsai, Kazakhstan: a study of solid and fluid inclusions in chromite. J. Petrol. 38, 1419–1458.
Montagnat, M., Blackford, J.R., Piazolo, S., Amaud, L., Lebensohn, R.A., 2011. Measurement and full-field predictions of deformation heterogeneities in ice. Earth Planet. Sci. Lett. 305, 153–160.
Moreno, T., Prichard, H., Gibbons, W., Lunar, R., 1999. Chemical distribution of PGE in the ultramafic massifs of the Cabo Ortegal Complex (NW Spain). In: Stanley, et al. (Eds.), Mineral Deposits: Processes to Processing. Balkema, Rotterdam, pp. 755–758.
Mungall, J.E., 2005. Magmatic geochemistry of the platinum-group elements. In: Mungall, J.E. (Ed.), Exploration from Platinum-Group Elements DepositsShort Course Series Vol. 35. Mineral. Assoc., Canada, pp. 1–34.
Nagaya, T., Wallis, S.R., Kobayasi, H., Michibayashi, K., Mizukami, T., Seto, Y., Miyake, A., Matsumoto, M., 2014. Dehydration breakdown of antigorite and the formation of B-type olivine CPO. Earth Planet. Sci. Lett. 387, 67–76.
Nakagawa, M., Franco, H.E.A., 1997. Placer Os–Ir–Ru alloys and sulfides: indicators of sulfur fugacity in an ophiolite? Can. Mineral. 35, 1441–1452.
Naldrett, A., Duke, J.M., 1980. Pt metals in magmatic sulfide ores. Science 208, 1417–1424.
Naldrett, A.J., Lehmann, J., 1988. Spinel non-stoichiometry as the explanation for Ni, Cu-, and PGE-enriched sulphides in chromitites. In: Prichard, H.M., Potts, P.J., Bowles, J.F.W., Cribbs, S.J. (Eds.), Geoplatinum '87, London, pp. 93–110.
Naldrett, A.J., Lehmann, J., Augé, T., 1989. Reactions between non-stoichiometric chromite and sulfide as the explanation for Ni Cu and PGE-enriched sulphides: examples from layered intrusion and ophiolites. Magmatic Sulfide Conf., 5th, Harare, Zimbabwe, Proc.
Norman, M., Pearson, N., Sharma, A., Griffin, W., 1996. Quantitative analysis of trace elements in geological materials by laser ablation ICPMS: instrumental operating conditions and calibration values of NIST glasses. Geostand. Newslett. 20 (2), 247–261.
Norman, M., Griffin, W., Pearson, N., Garcia, M., O'Reilly, S., 1998. Quantitative analysis of trace element abundances in glasses and minerals: a comparison of laser ablation inductively coupled plasma mass spectrometry, solution inductively coupled plasma mass spectrometry, proton microprobe and electron microprobe data. J. Anal. At. Spectrom. 13, 477–482.
Pagé, P., Barnes, S.J., 2009. Using trace elements in chromites to constrain the origin of podiform chromitites in the Thetford Mines ophiolite, Québec, Canada. Econ. Geol. 104, 997–1018.
Pagé, P., Barnes, S.J., Bédard, J.H., Zientek, M.I., 2012. In situ determination of Os, Ir, and Ru in chromites formed from komatiite, tholeiite and boninite magmas: implications for chromite control of Os, Ir and Ru during partial melting and crystal fractionation. Chem. Geol. 302–303, 3–15.
Peregoedova, A., Ohnenstetter, M., 2002. Collectors of Pt, Pd, and Rh in a S-poor Fe–Ni–Cu sulfide system at 760 °C: experimental data and application to ore deposits. Can. Mineral. 40, 527–561.
Peregoedova, A., Barnes, S.-J., Baker, D.R., 2004. The formation of Pt–Ir alloys and Cu–Pd-rich sulfide metls by partial desulfurization of Fe–Ni–Cu sulphides: results of experiments and implications for natural systems. Chem. Geol. 208, 247–264.
Piña, R., Gervilla, F., Barnes, S.-J., Ortega, L., Lunar, R., 2015. Liquid immiscibility between arsenide and sulfide melts: evidence from a LA-ICP-MS study in magmatic deposits at Serranía de Ronda (Spain). Miner. Depos. 50 (3), 265–279.
Plank, T., Ludden, J.N., 1992. Geochemistry of sediments in the Argo abyssal plain at Site 765: a continental margin reference section for sediment recycling in subduction zones. Proc. Ocean Drill. Program Sci. Results 123, 167–189.
Prichard, H.M., Ixer, R.A., Lord, R.A., Maynard, J., Williams, N., 1994. Assemblages of platinum-group minerals and sulfides in silicate lithologies and chromite-rich rocks within the Shetland ophiolite. Can. Mineral. 32, 271–294.
Prichard, H.M., Neary, C.R., Fisher, F.C., O'Hara, M.J., 2008. PGE-rich podiform chromitites in the Al'Ays ophiolite complex, Saudi Arabia: an example of critical mantle melting to extract and concentrate PGE. Econ. Geol. 103, 1507–1529.
Prichard, H.M., Barnes, S.J., Godel, B., Reddy, S.M., Bukmanovic, Z., Halfpenny, A., 2015. The structure and origin of nodular chromite from the Troodos ophiolite, Cyprus, revealed using high-resolution X-ray computed tomography and Electron Backscattered Diffraction. Lithos 218–219, 87–98.
Proenza, J.A., Zaccarini, F., Escayola, M., Cábana, C., Schalamuk, A., Garuti, G., 2008. Composition and textures of chromite and platinum-group minerals in chromitites of the western ophiolitic belt from Córdoba Pampean Ranges, Argentine. Ore Geol. Rev. 33, 32–48.
Rabbia, O.M., Alfaro, G., Barra, F., 1994. Presencia de espilitas metasomatizadas en el cinturón serpentinítico de la Cordillera de la Costa. Jornada de Mineralogía, Petrografía y Metalogénesis de rocas Ultrabásicas Vol. 2(3), pp. 607–615.
Reich, M., Kesler, S.E., Utsunomiya, S., Palenik, C.S., Chryssoulis, S.L., Ewing, R.C., 2005. Solubility of gold in arsenian pyrite. Geochim. Cosmochim. Acta. 69, 2781–2796.
Reich, M., Utsunomiya, S., Kesler, S.E., Wang, L.M., Ewing, R.C., Becker, U., 2006. Thermal behavior of metal nanoparticles in geologic materials. Geology 34, 1033–1036.
Ribeiro da Costa, I., Barriga, F.J.A.S., Viti, C., Mellini, M., Wicks, F., 2008. Antigorite in deformed serpentinites from the Mid-Atlantic Ridge. Eur. J. Mineral. 20, 563–572.
Richter, R.P., Ring, U., Willner, P.A., Leiss, B., 2007. Structural contacts in subduction complexes and their tectonic significance: the Late Paleozoic coastal accretionary wedge of Central Chile. J. Geol. Soc. 164, 203–214.
Rüpke, L.H., Morgan, J.P., Hort, M., Connolly, J.A.D., 2004. Serpentine and the subduction zone water cycle. Earth Planet. Sci. Lett. 223, 17–34.
Sack, R.O., Ghiorso, M.S., 1991. Chromian spinels as petrogenetic indicators: thermodynamic and petrological applications. Am. Mineral. 76, 827–847.
Salazar, E.A., 2015. Geoquímica y mineraloíía de los cuerpos serpentiniticos del complejo ofiolítica del centro-sur de Chile. Ph.D Thesis (unpublished), Universidad de Chile, Chile, 124 pp.
Salters, V.J.M., Stracke, A., 2004. Composition of the depleted mantle. Geochem. Geophys. Geosyst. 5 (5), Q05B07. http://dx.doi.org/10.1029/2003GC000597.
Satsukawa, T., Piazolo, S., González-Jiménez, J.M., Colás, V., O'Reilly, S.Y., Gervilla, F., Fanlo, I., Kerestedjian, T.N., 2015. Fluid-present deformation aids chemical modification of chromite: insights from chromite from Golyamo Kamneyane, SE Bulgaria. Lithos 228–229, 78–89.
Schirra, W. 1991. Die sudliche Kusten kordillere Chiles: Ein palaozoischer Ophiolith komplex des 'ensialic mature marginal basin'-Typs mit Kieslagervorkommen. Ph.D. Thesis (Unpublished), University of Heidelberg, 238 pp.
Schmidt, K., Koschinsky, A., Garbe-Schönberg, D., de Carvalho, L.M., Seifert, R., 2007. Geochemistry of hydrothermal fluids from the ultramafic-hosted Logatchev hydrothermal field, 15°N on the Mid-Atlantic Ridge: temporal and spatial investigation. Chem. Geol. 242 (2), 1–21.
Shabani, T.A.A., 2009. Mineral chemistry of chlorite replacing biotite from granitic rocks of the Canadian Appalachians. J. Sci. Islamic Rep. Iran 20, 265–275.
Shi, R., Alard, O., Zhi, X., O'Reilly, S.Y., Pearson, N.J., Griffin, W.L., Zhang, M., Chen, X., 2007. Multiple events in the NeoTethyan oceanic upper mantle: evidence from Ru–Os–Ir alloys in the Luobusa and Dongqiao ophiolitic podiform chromitites. Tibet. Earth Planet. Sci. Lett. 261, 33–48.
Singh, A.K., Devi, L.D., Singh, N.I., Subramanyam, K.S.V., Singh, R.B., Satyanarayanan, M., 2013. Platinum-group elements and gold distributions in peridotites and associated podiform chromitites of the Manipur ophiolitic complex, Indo-Myanmar Orogenic Belt, Northeast India. Chem. Erde-Geochem. 73 (2), 147–161. http://dx.doi.org/10.1016/j.chemer.2012.07.004.
Stipp, M., Stünitz, H., Heilbronner, R., Schmid, S.M., 2002. The eastern Tonale fault zone: a "natural laboratory" for crystal plastic deformation of quartz over a temperature range from 250 to 700 °C. J. Struct. Geol. 24, 1861–1884.
Stockman, H.W., Hlava, P.F., 1984. Platinum-group minerals in Alpine chromitites from southwestern Oregon. Econ. Geol. 79, 492–508.
Svahnberg, H., Piazolo, S., 2012. The initiation of strain locallisation in plagioclase-rick rocks: insights from detailed microstructural analyses. J. Struct. Geol. 32 (10), 1404–1416.
Tarkian, M., Naidenova, E., Zhelyaskova-Panayotova, M., 1991. Platinum-group minerals in chromitites from the Eastem Rhodope Ultramafic Complex, Bulgaria. Mineral. Petrol. 44, 73–87.
Testafaye, F., Taskinen, P., 2010. Sulfide mineralogy—literature review. Aalto University Publications in Materials Science and Engineering Aalto-yliopiston materiaalitekniikan julkaisuja (54 pp.).
Thalhammer, O.A.R., Prochaska, W., Mühlhans, H.W., 1990. Solid inclusions in chrome-spinels and platinum group element concentrations from the Hochgrössen and Kraubath ultramafic massifs (Austria). Contrib. Mineral. Petrol. 105, 66–80.
Thayer, T.P., 1942. Chrome resources of Cuba. U.S. Geol. Surv. Bull. 935-A (74 pp.).
Torres-Ruiz, J., Garuti, G., Gazzotti, M., Gervilla, F., Fenoll Hach-Alí, P., 1996. Platinum-group minerals in chromitites from the Ojen lherzolite massif (Serranía de Ronda, Betic Cordillera, Southern Spain). Mineral. Petrol. 56, 25–50.
Trommsdorff, V., Evans, B.W., 1972. Progressive metamorphism of antigorite schists in the Bergell Tonalite Aureole (Italy). Am. J. Sci. 272, 423–437.
Trommsdorff, V., Evans, B.W., 1974. Alpine metamorphism of peridotitic rocks. Schweiz. Mineral. Petrogr. Mitt. 54, 333–352.

Tsoupas, G., Economou-Eliopoulos, M., 2008. High PGE contents and extremely abundant PGE-minerals hosted in chromitites from the Veria ophiolite complex, northern Greece. Ore Geol. Rev. 33, 3–19.

Urai, J., Means, W.D., Lister, G.S., 1986. Dynamic recrystallization of minerals. In: Heard, H.C., Hobbs, B.E. (Eds.), Mineral and Rock Deformation: Laboratory Studies, the Paterson VolumeGeophys. Monogr. Vol. 36. Am. Geophys. Union, Washington D.C., pp. 161–200.

Uysal, I., Tarkian, M., Sadiklar, M.B., Zaccarini, F., Meisel, T., Garuti, G., Heidrich, S., 2009. Petrology of Al- and Cr-rich ophiolitic chromitites from the Muğla, SW Turkey: implications from composition of chromite, solid inclusions of platinum-group mineral, silicate, and base-metal mineral, and Os-isotope geochemistry. Contrib. Minerl. Petrol. 158, 659–674.

Vergara, L., 1970. Prospección de yacimientos de cromo y hierro en La Cabaña, Cautín. Memoria de Título, Universidad de Chile. Departamento de Geología (96 pp.).

Vivallo, W., Alfaro, G., Díaz, L., 1988. Los metabasaltos de la Serie Occidental de la Cordillera de la Costa entre los 38°–41° latitud Sur, Chile: evidencias geoquímicas de cuenca marginal durante el Paleozoico. Congresso Latinoamericano de Geología Vol. 7(1), pp. 260–273.

Willner, A.P., 2005. Pressure–temperature evolution of a Late Palaeozoic paired metamorphic belt in North-Central Chile (34°–35°30′S). J. Petrol. 46, 1805–1833. http://dx.doi.org/10.1093/petrology/egi035.

Willner, A.P., Pawlig, S., Massonne, H.-J., Hervé, F., 2001. Metamorphic evolution of spessartine quartzites (coticules) in the high-pressure, low-temperature complex at Bahia Mansa, Coastal Cordillera of south-central Chile. Can. Mineral. 39, 1547–1569.

Willner, A.P., Thomson, S.N., Kröner, A., Wartho, J., Wijbrans, J.R., Hervé, F., 2005. Time markers for the evolution and exhumation history of a Late Palaeozoic paired metamorphic belt in North-Central Chile (34°–35°30′S). J. Petrol. 46, 1835–1858. http://dx.doi.org/10.1093/petrology/egi036.

Wood, S.A., 2002. The aqueous geochemistry of the platinum-group elements with applications to ore deposits. In: LJ (Ed.), The Geology, Geochemistry, Mineralogy and Mineral Beneficiation of Platinum-Group Elements. Canadian Institute of Minning, Metallurgy and Petroleum, Canada, pp. 211–249.

Yang, K., Seccombe, P.K., 1993. Platinum-group minerals in the chromitites from the Great Serpentine Belt, NSW, Australia. Mineral. Petrol. 47, 263–286.

Yund, R.A., 1962. The system Ni–As–Si phase relations and mineralogic significance. Am. J. Sci. 260, 761–782.

Zane, A., Weiss, Z., 1998. A procedure for classification of rock-forming chlorites based on microprobe data. Rend. Fis. Accad. Lincei 9, 51–56.

Zane, A., Sassi, R., Guidotti, C.V., 1998. New data on metamorphic chlorite as a petrogenetic indicator mineral, with special regard to greenchist-facies rocks. Can. Mineral. 36, 713–726.

Zang, W., Fyfe, W.S., 1995. Chloritization of the hydrothermally altered bedrock at the Igarapé Bahia gold deposit, Carajás, Brazil. Mineral. Deposita 30, 30–38.